

## Event-driven piezoelectric energy harvesting for railway field applications

Shuai Qu<sup>a,b</sup>, Yuhao Ren<sup>a</sup>, Guobiao Hu<sup>c,\*</sup>, Wei Ding<sup>d,b</sup>, Liwei Dong<sup>e</sup>, Jizhong Yang<sup>f</sup>, Zaixin Wu<sup>g</sup>, Shengyang Zhu<sup>a</sup>, Yaowen Yang<sup>b,\*</sup>, Wanming Zhai<sup>a</sup>

<sup>a</sup> Train and Track Research Institute, State Key Laboratory of Rail Transit Vehicle System, Southwest Jiaotong University, 610031 Chengdu, China

<sup>b</sup> School of Civil and Environmental Engineering, Nanyang Technological University, 639798, Singapore

<sup>c</sup> Internet of Things Thrust, The Hong Kong University of Science and Technology(Guangzhou), Guangzhou, China

<sup>d</sup> School of Mechanical Engineering and State Key Laboratory of Strength & Vibration of Mechanical Structures, Xi'an Jiaotong University, Xi'an 710049, China

<sup>e</sup> Institute of Rail Transit, Tongji University, Shanghai 201804, China

<sup>f</sup> China Railway Eryuan Engineering Group Co.,LTD, Chengdu, China

<sup>g</sup> Sichuan Shudao New System Rail Group Co.,LTD, Chengdu, China

### HIGHLIGHTS

- An improved vehicle-track coupled dynamic model uncovers previously unexplored intricate characteristics of rail vibrations.
- A novel event-driven enhancement method is proposed to maximize the energy collected across varying rail-line conditions.
- Cluster analyses are performed to identify representative configurations for streamlining design complexity.
- The robustness of representative designs is validated across diverse railway scenarios.

### ARTICLE INFO

#### Keywords:

Energy harvesting  
Piezoelectric  
Vehicle-track coupled dynamics  
Cluster analysis  
Intelligent optimization

### ABSTRACT

Piezoelectric energy harvesters (PEHs) hold promises for revolutionizing railway structural health monitoring (SHM). However, the challenges of designing high-robust PEHs for handling complex and ever-shifting vibrations in practical railway scenarios remain formidable. Unlike conventional methods that align the fundamental frequency of the PEH with the dominant frequency of the vibration source, this study employs an event-driven enhancement method. This study commences by employing a high-fidelity dynamic model of the PEH and an advanced vehicle-track coupled dynamic model to evaluate energy harvesting efficiency across various railway scenarios. The vehicle-induced track vibrations are predicted across various train speeds, track structures, and track irregularities, considering 12 distinct vehicle-track conditions and totaling 3600 simulation datasets, each representing a specific event. We employ the particle swarm optimization (PSO) algorithm to identify optimal PEH designs for different events. To streamline this process, instead of offering one optimal solution for each event, we employ the K-means algorithm to cluster similar events. Subsequently, we choose the centroid design for each cluster as the representative solution for events within that cluster. This approach allows us to use a limited number of representative PEHs to effectively address most events across different clusters. Finally, we thoroughly examine and evaluate the dynamic responses of these representative designs to demonstrate their robust performance. This study explores PEH design optimization from a fresh perspective, bridging the gap between theoretical design and practical implementation in rail transportation systems.

### 1. Introduction

The surge in rail transportation has led to a significant extension of railway tracks. In the years ahead, the development focus will shift from massive construction efforts to intelligent operation procedures,

maintenance practices, and health monitoring of railways [1,2]. This transition will necessitate the deployment of millions and even billions of sensing and communication devices along railway networks to ensure their safe and efficient operation [3–5]. The conventional reliance on chemical batteries to power these devices has resulted in substantial

\* Corresponding authors.

E-mail addresses: [guobiaohu@hkust-gz.edu.cn](mailto:guobiaohu@hkust-gz.edu.cn) (G. Hu), [cwyyang@ntu.edu.sg](mailto:cwyyang@ntu.edu.sg) (Y. Yang).

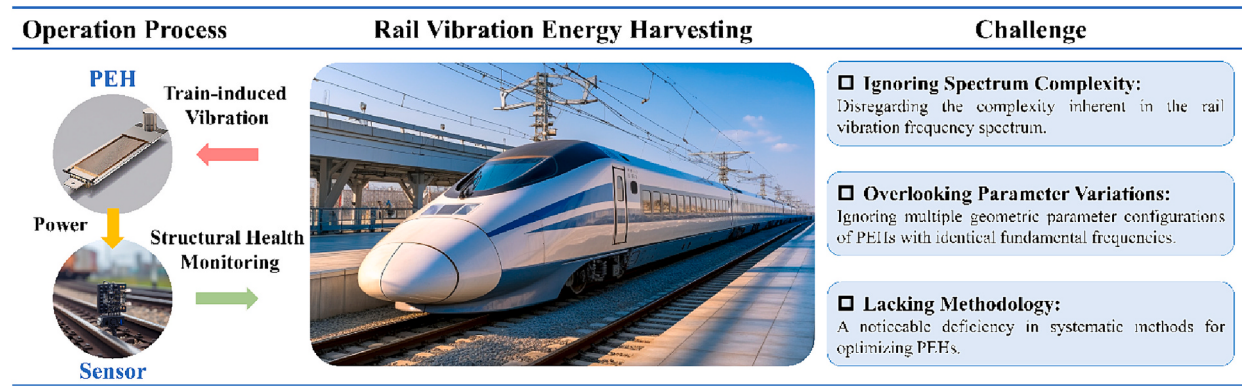


Fig. 1. Technical issues and challenges in harvesting rail vibration energy using PEH.

economic expenses and raised environmental concerns. Therefore, there is a pressing demand to explore alternative and sustainable energy sources for sensor systems alongside railways. Vibration energy harvesting has emerged as a promising solution capable of harnessing the abundant vibration energy in the ambient environment and converting it into electricity [6–8].

Recent years have witnessed extensive research on utilizing energy harvesters to power low-consumption monitoring systems along railway tracks [9–12]. Considerable efforts have been devoted to customizing and developing innovative energy harvesters for applications in railway systems, considering the unique environmental characteristics of various scenarios [5,13]. Notably, piezoelectric energy harvesters (PEHs) have garnered significant attention due to their compact sizes, ease of integration, and high power densities [14–16]. One common application in this field is the utilization of PEHs to harvest energy from track vibrations [17–21]. Different PEH designs have exhibited varying power generation capacities, with some studies reporting maximum power outputs in the milliwatt range [20,22]. Such power levels suggest that these PEHs have the potential to produce ample energy for real-time data collection and transmission, thereby aiding in track condition assessment and maintenance planning [23–25].

Among various PEH designs, one focus has been placed on examining cantilevered beams coated with piezoelectric patches due to their simple and robust structural configuration [26,27]. Typically, PEHs are designed for low-frequency applications, resulting in relatively large beam length-to-thickness ratios. Therefore, the Euler-Bernoulli beam theory has been widely adopted as a simplified yet effective approach for modeling PEHs [28,29]. More sophisticated models have been developed to account for the effects of rotary inertia and shear strains [26,28]. These include the Kirchhoff-Love plate models, which are more applicable for thin structures and have been used in tandem with the finite element method (FEM) and isogeometric analysis (IGA) to enhance modeling accuracy [30,31]. The Timoshenko beam theory, which incorporates the effects of rotary inertia and shear strain, has also been utilized to improve the accuracy of PEH modeling [32]. Existing research underscores the potential of PEHs to provide viable power solutions for wireless electronics, particularly when operating near their natural frequencies. Cantilevered beam designs in unimorph or bimorph configurations are particularly prevalent in this regard [33,34]. Regrettably, the narrow bandwidths of traditional PEHs have constrained their performance. This constraint has spurred a variety of inventive designs intended to enhance the efficiency of PEHs.

To address this challenge, researchers have embarked on the quest to diversify mechanisms in PEHs. They have proposed innovative designs to enhance the performance of PEHs by incorporating features such as flow-induced excitations [35–37], mechanical stoppers [38,39], spiral springs [40,41], multilayer piezoelectric transducers, ball-screw mechanisms [42], and magnetic masses [43–46]. These designs have demonstrated improved energy conversion efficiency, resulting in

higher output voltages and enhanced overall performance for various applications. In addition to piezoelectric energy harvesting, other transduction mechanisms, such as electromagnetic [47–49], triboelectric [39,50], and electrostatic [51], have also been explored. Some studies have even ventured into developing hybrid energy harvesting systems by combining two or more of these transduction mechanisms [52,53]. A composite piezoelectric-electromagnetic device proposed by Han et al. [54] exemplifies the advancement in hybrid energy harvesting technology. Their design offered a self-powered sensing solution for vehicle monitoring, which underscored the potential of integrated approaches in enhancing the efficiency and sustainability of transportation system operations. These hybrid systems leverage the strengths of multiple transduction mechanisms to boost power outputs and energy conversion efficiency. Moreover, prior studies have pioneered the development of self-powered triboelectric accelerometers for railway health monitoring. Their findings have validated the feasibility of harnessing vibration energy for powering wireless sensor network nodes [12,55]. Self-powered wireless sensor networks hold significant promise for monitoring railway tracks, potentially leading to reduced maintenance expenses and improved safety and reliability of railway transportation systems [24,25].

Empirical studies have validated that employing well-designed PEHs in railway systems for continuous or intermittent self-powered measurements and health monitoring is technically viable. However, delving into the realm of railway vibration energy harvesting poses persistent challenges, as depicted in Fig. 1. A significant limitation observed in most previous PEH designs is their narrow operation bandwidths. Despite some initiatives that aim to widen this range, PEHs still show remarkable sensitivity to even minor fluctuations in rail vibrations [56]. Moreover, existing design methodologies primarily focus on adjusting the harvester's resonant frequency to match a specific target, typically the dominant excitation frequency. However, singular excitation events may simultaneously coincide with numerous viable configurations, many of which potentially span multiple events. The extant designs largely bypass the adaptability and versatility of these configurations. Compounding these issues is a discernible methodological gap, and no comprehensive studies have ever been carried out to address these concerns. Therefore, a robust and adaptable PEH enhancement method is imperative to maximize energy harvesting efficiency by taking account of the intricacies of rail vibrations, thereby bridging the gap between laboratory research on PEHs and practical applications. In this regard, a recent work by Peralta et al. [57] represented a significant advancement in applying classical mathematical modeling techniques, specifically optimization and clustering analysis, to energy harvesting. Their innovative approach involved optimizations centered around various representative acceleration events, then clustering the outcomes

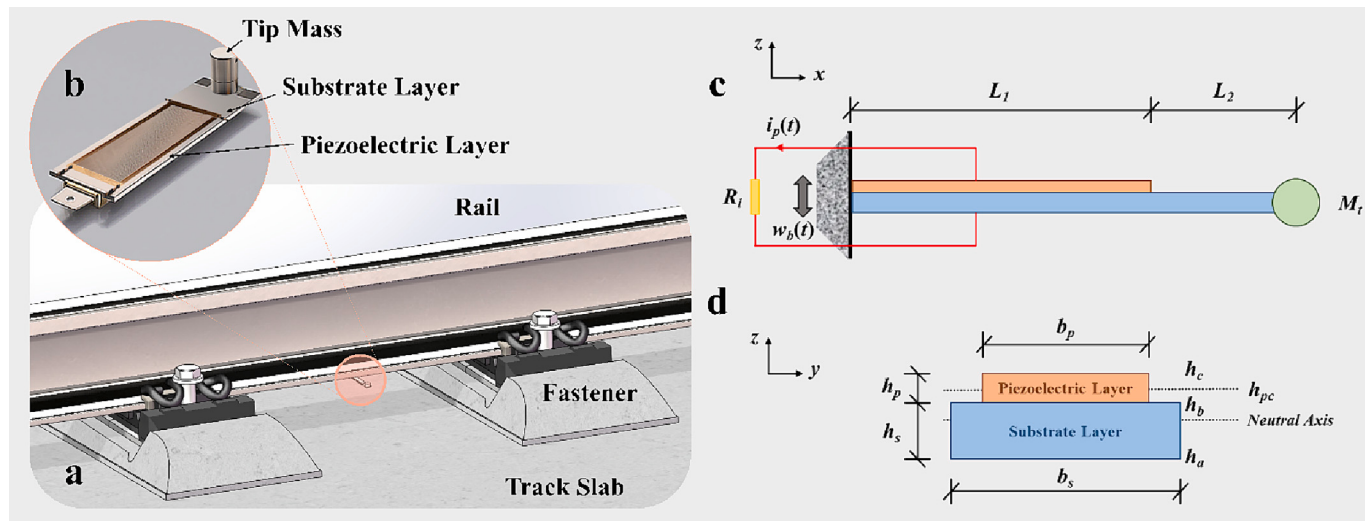


**Fig. 2.** The architecture of the piezoelectric energy harvester, i.e., a cantilevered piezoelectric beam consisting of a piezoelectric layer bonded to a main substructure: (a) installation location of PEH in actual railway scenarios; (b) detailed view of PEH; (c) side view of PEH structural schematic; (d) end view of PEH structural schematic.

to identify several optimal candidates. The framework proposed in [57] represents a generic method applicable across diverse design scenarios.

In this work, we introduce an advanced vehicle-track spatially coupled dynamics model that can unveil the intricate characteristics of rail vibrations, which is a pivotal aspect that has been notably absent in the previous rail vibration energy harvesting research. Leveraging this pioneering foundation, we employ an event-driven PEH enhancement method proposed in [57] and adapt it to address our specific challenge within the railway track vibration scenario. The optimization process involves the identification of optimal designs for a representative subset of events, followed by the clustering of optimal candidates to pinpoint the most promising solutions. The performance of these selected designs is subsequently assessed through continuous vibration energy harvesting. Furthermore, by retracing the rail vibration events corresponding to the results obtained from cluster analysis, this study offers a deep insight into the underlying rationale of the cluster analysis from the perspective of the spectral components of rail vibrations. These analyses uncover the critical factors related to rail-line conditions that significantly influence the design parameters of PEHs. Ultimately, our study evaluates the robustness of various PEH configurations across diverse railway scenarios. The most suitable design for powering rail-side sensing systems is identified by comparing the output power density of these potential configurations, showcasing their significant adaptability in a broad spectrum of railway scenarios.

The subsequent sections of this paper are organized as follows. **Section 2** introduces the proposed event-driven enhancement method tailored for PEH applications in railway vibration energy harvesting. **Section 3** presents the formulation of a distributed parameter model for a partially covered PEH and an advanced vehicle-track spatially coupled dynamics model. In **Section 4**, a comprehensive analysis is presented, delving into the characteristics of excitations in the examined scenarios based on a representative sample of rail vibration events. **Section 5** conducts a cluster analysis and a rigorous performance assessment, serving as a validation of the proposed optimization framework. Finally, **Section 6** summarizes the conclusions derived from this study.

## 2. Event-driven PEH optimization strategy

### 2.1. Overview of PEH design

The main focus of this study is to optimize a vibration energy harvester and examine its energy harvesting performance, making it

suitable for practical railway track applications. As shown in **Fig. 2(a)**, the energy harvesting system is fixed on the rail at the mid-span position between two rail fasteners using a clamer, and it is excited by rail vibrations. As can be seen in **Fig. 2(b)**, the PEH device comprises three modules: the piezoelectric layer, the substrate layer, and the tip mass. The piezoelectric cantilever beam is the key component to convert vibration energy into electricity. Train-induced vibrations provoke the resonance of the piezoelectric cantilever beam, leading to the generation of alternating mechanical stress in the piezoelectric material and, thus, voltage because of the piezoelectric effect. The theoretical model for describing this process will be elaborated on in **Section 3.1**. The PEH is mounted to the rail via a bolt connection. Thus, the vibrations present in the railway track can propagate and transfer to the PEH. The circuit module connects to the piezoelectric patch and regulates the harvested current, effectively supplying power to the sensing and communication modules.

**Fig. 2(c)** shows the schematic of the PEH. The left side of the beam is clamped to the base. The thickness and length of the host beam are  $h_s$  and  $L_s$  ( $L_s = L_1 + L_2$ ). The host is covered by a piezoelectric layer of thickness  $h_p$  and length  $L_p$  ( $L_p = L_1$ ). The piezoelectric transducer is shunted to a resistive load  $R_l$ . The subscripts  $s$  and  $p$  denote the host beam and the piezoelectric layer, respectively. The subscripts 1 and 2 represent the segments with and without the piezoelectric layer, respectively. A concentrated mass  $M_t$  is attached at the tip of the beam to tune its fundamental natural frequency. **Fig. 2(d)** shows the cross-sectional view of the beam, where  $h_a$  is the position of the bottom of the substrate layer to the neutral axis. The widths of the host beam and the piezoelectric layer are  $b_s$  and  $b_p$ , respectively.  $h_b$  and  $h_c$  are the positions of the bottom and top of the piezoelectric layer to the neutral axis, respectively.  $h_{pc}$  is the position of the center of the piezoelectric layer to the neutral axis [58].

### 2.2. Event-driven optimization strategy

In developing our optimization strategy for harvesting vibration energy from railway tracks, we build upon the conceptual framework established by Peralta et al. [57] and extend it to tackle the specific challenges presented in the railway context. Our strategy, which also uses the optimization algorithm and clustering analysis as in [57], is specifically adapted to accommodate the wide frequency band and strong stochastic characteristics of railway vibrations. In general, it consists of four tailored steps:

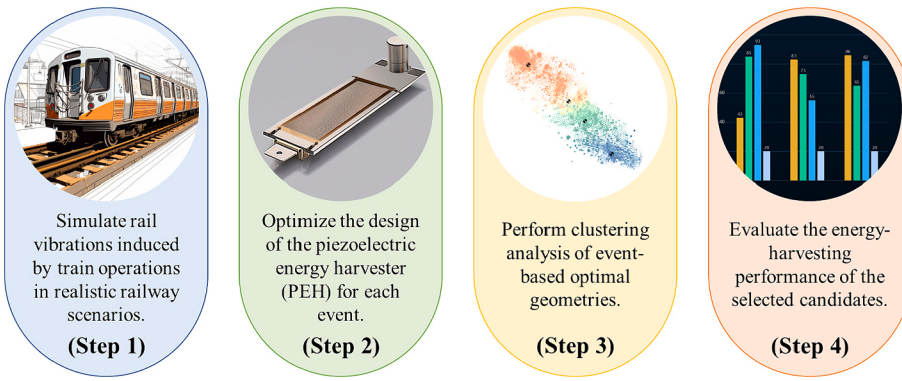


**Fig. 3.** Overview of the proposed event-driven optimization strategy.

**Step 1.** Simulate rail vibrations induced by train operations in realistic railway scenarios and generate a sample database (each data is referred to as an event in this study);

**Step 2.** Optimize the design of the piezoelectric energy harvester (PEH) for each event;

**Step 3.** Perform clustering analysis of event-driven optimal geometries and classify the design candidates;

**Step 4.** Evaluate the energy-harvesting performance of the candidates obtained through clustering analysis over long time windows.

The purpose of **Step 1** is to simulate the dynamic responses of wheel-rail coupled systems during train operations on railway tracks. The vibrations in the vehicle-track coupled system are primarily caused by disturbances in the wheel-rail system. An event-driven sample database can be obtained by performing dynamic numerical simulations of rail vibrations considering track irregularities of different track spectra. This database allows for inferring the variability in optimal geometries considering a relatively large number of events, with rail vibration acceleration for each working condition referred to as an individual event. The rail excitations database will be presented in [Section 4](#).

Geometry optimization in **Step 2** is independently performed for each event, with a total of  $N_{event}$  events being considered. In the schematic view shown in **Step 3** of [Fig. 3](#), each dot represents the optimal design variables  $\mathbf{g}_i$  independently obtained for each event. The objective function can be modified; for instance, the optimization in this study considers energy per unit mass. In the current research, six design variables are considered, including:

$$\mathbf{g}_i = \{L_s, l, h, b_s, w, M_t\} \quad (1)$$

where  $L_s$  represents the substrate length;  $l$  denotes the ratio of piezoelectric layer length to the substrate length ( $l = L_p/L_s$ );  $h$  stands for the ratio of the piezoelectric thickness to the substrate thickness ( $h = h_p/h_s$ );  $b_s$  denotes the substrate width;  $w$  refers to the ratio of the piezoelectric layer width to the substrate beam width ( $w = b_p/b_s$ ); and  $M_t$  is the concentrated mass at the free end of the piezoelectric cantilever beam. Subsequently, the Particle Swarm Optimization (PSO) method will be employed to optimize each individual event.

Evaluating the performance of a PEH involves comparing its output voltage and/or power, which is an effective indicator in dealing with simple harmonic external excitations. However, the vibration spectrum of the rail is broad and complex due to track irregularity and vehicle-track coupling, resulting in broadband excitations and making rail vibration energy harvesting challenging. Prior research suggested that simply adjusting the natural frequency of the PEH to match the dominant fundamental excitation frequency may not yield the maximum energy [57]. Thus, to ensure that the PEH can harness the maximum energy, choosing the harvested energy density as the performance indicator in the optimization study is more reasonable. In this section, the optimization problem for a single event is formulated as

$$\mathbf{g}_{obj} = \arg \max_{\substack{\mathbf{g}_i \in \mathbf{G} \\ \mathbf{e}_i \in \text{Event}}} |f(\mathbf{g}_i | \mathbf{e}_i)| \quad (2)$$

The objective function  $f(\mathbf{g}_i | \mathbf{e}_i)$  represents the energy density, defined as the total energy harvested by a PEH divided by its total mass. Efficient evaluation of PEH performance is facilitated through energy density, a pivotal performance indicator in the optimization process [59,60]. Computing the total harvested energy by integrating the output voltage over time while considering the optimal load resistance for each PEH configuration enables a comprehensive assessment of energy harvesting efficiency. The total mass of the PEH is determined by three essential components: the cantilever substrate, the piezoelectric element, and the tip mass. This chosen metric is aimed at prioritizing efficiency in compact and lightweight designs, a crucial aspect in practical energy harvesting scenarios. To study the variations in optimal geometries arising from different events, we employ the PSO method to optimize each event with a population of thirty particles. PSO is an effective metaheuristic algorithm inspired by the social behavior of birds flocking and fish schooling, particularly well-suited for solving non-convex problems, such as those involving nonlinear, multimodal, and high-dimensional search spaces [61]. The iterative nature and computational efficiency of the PSO algorithm make it a popular choice for complex optimization problems.

In the process of optimizing the geometric parameters of the PEH based on events, choosing the external electrical resistance ( $R_l$ ) requires special attention due to its significant impact on power generation, as discussed in other works [18]. In this regard, when assessing the fitness of particles using the objective function,  $f(\mathbf{g}_i | \mathbf{e}_i)$ , the electrical resistance should be chosen to maximize the output energy. The essence of the optimization study in this paper is to tune the natural frequency of the PEH by changing the geometric parameters, making it produce the maximum energy under different events. Therefore, it is easy and straightforward that we can find the optimal load resistance by calculating and comparing the power outputs of the PEH connected to different load resistances. This optimization problem can be expressed as:

$$R_l^{optimal} = \arg \max_{\omega \in \Omega, R_l \in \mathbf{R}} |P(\omega, R_l | \mathbf{g}_i)| \quad (3)$$

where  $P(\omega, R_l | \mathbf{g}_i)$  is the output power of the PEH. In [Section 3.1](#), the distributed parameter model of the PEH under random excitation was derived. Thus, we can easily obtain the output voltage  $V(\omega, R_l | \mathbf{g}_i)$  of the PEH by replacing  $A_{Rail}$  in Eq. (4) with harmonic excitation  $A_{ce}e^{j\omega t}$ , and thus the output power  $P(\omega, R_l | \mathbf{g}_i)$ .

$$V(\omega, R_l | \mathbf{g}_i) = \frac{\sum_{r=1}^{\infty} \chi_r \frac{j\omega \gamma_r A_{ce}}{\omega_r^2 - \omega^2 + j2\zeta_r \omega_r \omega}}{\left\{ \left( \frac{1}{R_l} + j\omega C_p \right) + \sum_{r=1}^{\infty} \frac{j\omega \chi_r^2}{\omega_r^2 - \omega^2 + j2\zeta_r \omega_r \omega} \right\}} \quad (4)$$

$$P(\omega, R_l | \mathbf{g}_i) = \frac{V^2(\omega, R_l | \mathbf{g}_i)}{R_l} \quad (5)$$

The procedure is then used in the subsequent optimization processes to ensure consistency between the results. It should also be noted that the working stress and deformation should be controlled within a safe range to avoid material brittleness and fatigue, which were conservatively set at 60% of the material's ultimate thresholds (276 MPa for stress and 0.002 for strain). This was achieved through a meticulous verification process during optimization, where each PEH design was rigorously assessed against these limits for each excitation event. This approach not only verifies the geometric configuration of the cantilever beams within the strength limit of the material but also ensures the resilience and integrity of the PEH design under diverse and demanding operational conditions.

The objective of **Step 3** is to address the variability of the optimal geometries and to find the optimal candidates. This step is referred to as clustering and candidate identification. The optimal design for each event tends to have a natural frequency close to the primary frequency of rail vibrations. Consequently, it is possible to group them into clusters based on the geometrical parameters (design variables) using the K-means algorithm [62]. The clustering analysis divides the optimal geometries into groups based on their similarities. The Silhouette Method is incorporated to identify the most suitable cluster number [63].

Upon obtaining the clustering result, the cluster centroid is considered the representative candidate of each cluster. In **Step 3** of Fig. 3, optimal designs are grouped into several clusters highlighted in different colors with their centroids indicated by black crosses. Each cluster is represented by a centroid with a minimized average distance to the assigned elements in the group. These centroids provide a concise representation of the design space, thereby reducing the complexity of the optimization problem. The optimal solutions are drastically reduced from thousands of potential combinations to only several centroid candidates. The selected candidate solutions will be further evaluated and compared to identify optimal candidates to tackle the typical scenarios.

The final step, **Step 4**, assesses the total energy collected by each candidate obtained in **Step 3** during the rail excitation period (or a specified time window). This step aims to select the design demonstrating the highest energy density in scenarios sharing common characteristics. The finally determined design is preferred in a real-life scenario because it can generate the maximum amount of energy independently of rail traffic. In **Step 4** of Fig. 3, the energy generated by selected candidates is shown schematically. This step will be demonstrated and explained via several numerical examples in **Section 5**.

Incorporating the optimization approach and clustering analysis into the design process enables exploring an extensive design space. It also provides a deeper understanding of the influences of the design parameters on the energy harvesting performance of the PEHs. By meticulously examining the variability in these optimal configurations, the robustness and universality of the solutions can be ensured. The synergy of these methods renders proficient balancing of trade-offs among multiple design objectives and constraints, leading to an optimal design that maximizes energy harvesting capabilities while complying with practical limitations and requirements.

### 3. Modeling and formulation

#### 3.1. Distributed parameter model for PEH

Although the distributed parameter model of a partially covered PEH is not brand new [58], the modeling process is retrospected and summarized for the sake of completeness and ease of understanding for readers from different backgrounds. The analytical model of the energy harvesting system is developed by taking into account the bidirectional electromechanical coupling behavior between the structure and shunt circuit [38,63,64]. Using the Euler-Bernoulli beam theory, the coupled

equations of motion for the PEH, for the segments with and without the piezoelectric layer, are written as

$$\left\{ \begin{array}{l} E_1 I_1 \frac{\partial^4 w_1(x_1, t)}{\partial x_1^4} + c_1^s I_1 \frac{\partial^5 w_1(x_1, t)}{\partial x_1^4 \partial t} + c_1^a \frac{\partial w_1(x_1, t)}{\partial t} + m_1 \frac{\partial^2 w_1(x_1, t)}{\partial t^2} + \\ \vartheta v(t) \times \left[ \frac{d\delta(x_1)}{dx_1} - \frac{d\delta(x_1 - L_1)}{dx_1} \right] = -m_1 \frac{\partial^2 w_b(t)}{\partial t^2} \\ E_2 I_2 \frac{\partial^4 w_2(x_2, t)}{\partial x_2^4} + c_2^s I_2 \frac{\partial^5 w_2(x_2, t)}{\partial x_2^4 \partial t} + c_2^a \frac{\partial w_2(x_2, t)}{\partial t} + m_2 \frac{\partial^2 w_2(x_2, t)}{\partial t^2} \\ = -[m_2 + M_b \delta(x_2 - L_2)] \frac{\partial^2 w_b(t)}{\partial t^2} \end{array} \right. \quad (6)$$

In this context,  $w_1(x_1, t)$  and  $w_2(x_2, t)$  denote the relative displacements to the base motion of the beam segments with and without the piezoelectric layer, respectively. The terms  $EI$ ,  $c^s$ ,  $c^a$ ,  $m$ ,  $M_b$ , and  $L$  represent the flexural rigidity of the beam ( $E$  as the elastic modulus and  $I$  as the area moment of inertia of the cross-section), strain rate damping, viscous air damping, distributed mass of the beam per unit length, concentrated mass at the free end, and substrate length along the  $x$ -axis, respectively.  $\delta(x)$  denotes the Dirac delta function.  $L_1$  signifies the length of the piezoelectric transducer, and  $C_p$  represents the piezoelectric internal capacitance. The electromechanical coupling term  $\vartheta$  is determined by the dimensions and piezoelectric properties of the transducer. The following equation describes the linear constitutive relation for the piezoelectric material,

$$D_e(x_1, t) = e_{31} S(x_1, t) + \varepsilon_{33}^S E_3(t) \quad (7)$$

where  $S(x_1, t)$  represents the bending strain,  $D_e(x_1, t)$  denotes the electric displacement, and  $\varepsilon_{33}^S$  stands for the permittivity at constant stress. The electric field in the piezoelectric transducer concerning the voltage across it can be expressed as  $E_3(t) = -v(t)/h_p$ . According to the Euler-Bernoulli beam theory, the average bending strain in the piezoelectric transducer can be represented as  $S(x_1, t) = -h_{pc} [\partial^2 w_1(x_1, t) / \partial x_1^2]$ . Consequently, Eq. (7) becomes

$$D_e(x_1, t) = e_{31} h_{pc} \frac{\partial^2 w_1(x_1, t)}{\partial x_1^2} - \varepsilon_{33}^S \frac{v(t)}{h_p} \quad (8)$$

By integrating the electric displacement over the electrode area and differentiating with respect to time, the current  $i_p(t)$  flowing out of the piezoelectric transducer can be determined,

$$i_p(t) = \vartheta \int_{x_1=0}^{L_p} \frac{\partial^3 w_1(x_1, t)}{\partial x_1^3 \partial t} dx_1 - C_p \frac{dv(t)}{dt} \quad (9)$$

where  $C_p = \varepsilon_{33}^S b L_p / h_p$  represents the internal capacitance of the piezoelectric transducer. The clamped boundary condition implies that  $\partial^2 w_1(0, t) / \partial x_1 \partial t$  at  $x_1 = 0$ . As a result, Eq. (9) becomes

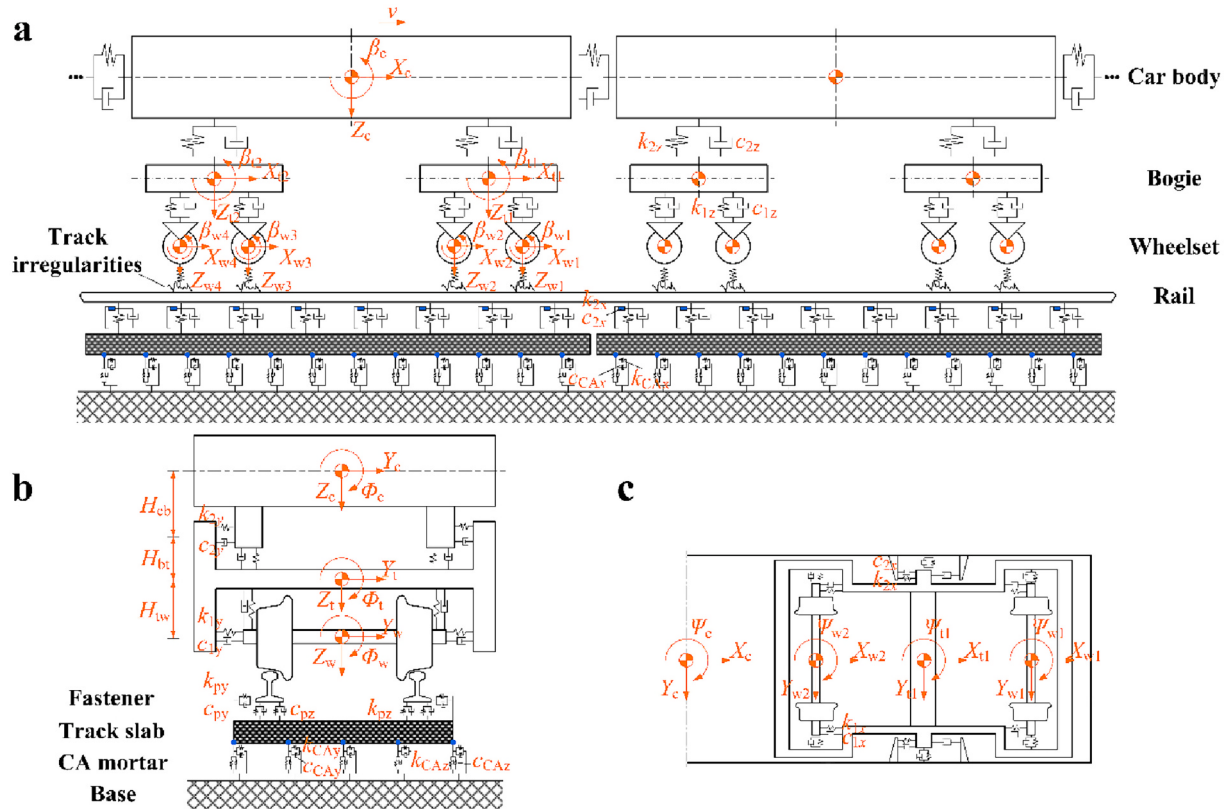
$$i_p(t) = \vartheta \frac{\partial^2 w_1(x_1, t)}{\partial x_1 \partial t} \Big|_{x_1=L_p} - C_p \frac{dv(t)}{dt} \quad (10)$$

Subsequently, the modal superposition method is employed to derive the closed-form solution of the electromechanically coupled equations, which considers the first three modal orders, helps simplify the analysis and enhances the efficiency of solving the coupled equations. To strike a balance between theoretical estimation and practical application, a uniform damping ratio of 0.008 is applied across the first three modes. This choice aligns with standard damping scenarios commonly associated with these materials. Although the PEH investigated in this study has a constant rectangular cross-section, the modeling of more complex irregular PEHs can also leverage the similar modal superposition method in conjunction with FEM.

**Table 1**

DOFs of each vehicle.

Vehicle component	Longitudinal motion	Lateral motion	Vertical motion	Roll motion	Pitch motion	Yaw motion
Car body	$X_c$	$Y_c$	$Z_c$	$\phi_c$	$\beta_c$	$\psi_c$
Bogie ( $i = 1-2$ )	$X_{ti}$	$Y_{ti}$	$Z_{ti}$	$\phi_{ti}$	$\beta_{ti}$	$\psi_{ti}$
Wheelset ( $i = 1-4$ )	$X_{wi}$	$Y_{wi}$	$Z_{wi}$	$\phi_{wi}$	$\beta_{wi}$	$\psi_{wi}$

**Fig. 4.** The spatial vehicle-track coupled dynamic model: (a) front view, (b) left side view and (c) top view.

### 3.2. Vehicle-track coupled dynamic model

The classical vehicle-track coupled dynamics model can accurately capture the vertical and lateral dynamic characteristics of the vehicle and track system [1,65]. Its reliability has been extensively validated through many field tests. Building on this foundation, Luo et al. [66] derived and solved the in-plane forced vibration equation for track slabs by considering the longitudinal coupling effect. They systematically introduced a three-dimensional theoretical model for analyzing train-slab track spatial interactions and compared the dynamic response differences between the proposed and conventional models. Therefore, in this study, we employ the advanced three-dimensional train-slab track spatially coupled model to compute vehicle-track interaction forces. In establishing the model, each vehicle is simplified as a four-axle mass-spring-damper system that comprises a car body, two bogies, four wheelsets, and two sets of suspension systems. This results in a total of 42 degrees of freedom (DOF), as illustrated in Table 1. The vehicle-track coupled dynamic model is depicted in Fig. 4.

The motion equations for each vehicle system component can be expressed in matrix form, resulting in a series of second-order differential equations in the time domain,

$$\mathbf{M}_v \ddot{\mathbf{X}}_v = \mathbf{F}_v \quad (11)$$

where  $\mathbf{M}_v$  is the mass matrix of the vehicle subsystem,  $\mathbf{X}_v$  the

displacement vector, and  $\mathbf{F}_v$  encompasses forces such as wheel-rail nonlinear interactions, suspension-generated forces, and gravitational effects. Detailed matrices and vectors are further explained in the Appendix A.

Based on the beam and rod dynamics theory, the model accounts for the longitudinal, torsional, lateral, and vertical vibrations of the rail. The axial and torsional vibrations of the rail are modeled as fixed-end constraint rods, and the bending vibrations of the rails are assumed to be simply supported Euler-Bernoulli beams. The motion equations of the track structure are solved using the modal superposition method (MSM). The original vibration equation is decoupled into a series of independent vibration equations by transforming the relationship between Cartesian and generalized coordinates. The dynamic responses of the system under each mode are then calculated. Detailed theoretical methods can be found in the reference [66].

To solve the large-scale dynamic system, we utilize the Zhai method [67], a fast explicit integration technique that provides stability, accuracy, and efficiency. A time step of  $1 \times 10^{-4}$  s is used for the wheel-rail dynamics problem. The integration formula is as follows,

$$\begin{cases} Z_{n+1} = Z_n + \dot{Z}_n \Delta t + \left(\frac{1}{2} + \varphi\right) \ddot{Z}_n \Delta t^2 - \varphi \ddot{Z}_{n-1} \Delta t^2 \\ \dot{Z}_{n+1} = \dot{Z}_n + (1 + \varphi) \ddot{Z}_n \Delta t - \varphi \ddot{Z}_{n-1} \Delta t \end{cases} \quad (12)$$

**Table 2**  
Train operating conditions contained in the rail vibration database.

Index	Train Speed	Track Type	Track Roughness	Count
1	120 km/h	MST	GR	
2	120 km/h	FST	GR	
3	100 km/h	MST	GR	
4	100 km/h	FST	GR	
5	120 km/h	MST	PR	Each working condition contains 300 sets of data.
6	120 km/h	FST	PR	
7	100 km/h	MST	PR	
8	100 km/h	FST	PR	
9	80 km/h	MST	PR	
10	80 km/h	FST	PR	
11	60 km/h	MST	PR	
12	60 km/h	FST	PR	

where  $Z$ ,  $\dot{Z}$ , and  $\ddot{Z}$  represent the displacement, velocity, and acceleration, respectively;  $\Delta t$  denotes the integral time step, and the subscript  $n$  signifies the time at  $t = n\Delta t$ ;  $\varphi$  and  $\psi$  are integral control parameters. Given the initial conditions of the system, the time-history dynamic responses of the vehicle-track coupled system can be computed stepwise using the integral recursive formula.

#### 4. Rail vibration database

Existing literature suggests that a higher output power can be achieved by matching the first two natural frequencies of the PEH with the first natural frequency of the rail and the wheel-rail coupled resonant frequency [17–19]. However, this design aims to collect energy from track vibrations under specific conditions and locations without full

consideration of the variability and complexity of the track vibration spectrum in real train operation scenarios [68]. Factors such as train speed, vehicle characteristic length, track characteristic length, and track geometry irregularities affect the rail vibration frequency [69–71]. Any changes in these factors may impact the vibration characteristics of the wheel-rail coupled system, resulting in a change of the rail vibration frequency and deteriorated PEH energy harvesting performance. Therefore, in the practical application of PEHs in harnessing rail vibration energy, it is essential to consider the complexity of the actual rail vibration spectrum.

#### 4.1. Dynamic parameters

Disturbances in the wheel-rail system are the fundamental cause of vibrations in the vehicle-track coupled system. Hence, it is crucial to understand the forms and morphological features of system excitation before generating a rail vibration database. To ensure that the generated rail vibration data can capture the complexity and variability in actual operational conditions, this study, based on advanced vehicle-track coupled dynamics theory, considers the effects of train speed, track type, and track irregularity on rail vibration. Numerical simulations were performed for 12 different operational conditions (Table 2), chosen to comprehensively represent the operation conditions that typically exist in subway systems. This diversity ensures that our analysis reflects real-world variability. Each condition was analyzed with 300 events, and the sample size was determined through convergence analysis to yield consistent clustering results, underscoring the robustness of our findings. In this context, MST denotes monolithic slab tracks, and FST refers to steel spring floating slab tracks. Two conditions of track irregularity are also considered: GR, an acronym for “good rail irregularity”, refers to simulation scenarios where track smoothness is relatively good; and PR stands for “poor rail irregularity”, which refers to situations where the track smoothness is notably poor. Further details on these two types of tracks and the track irregularities will be explained in the latter part of this section.

In actual railway line operations, railway operators determine specific speed requirements based on factors such as track conditions,

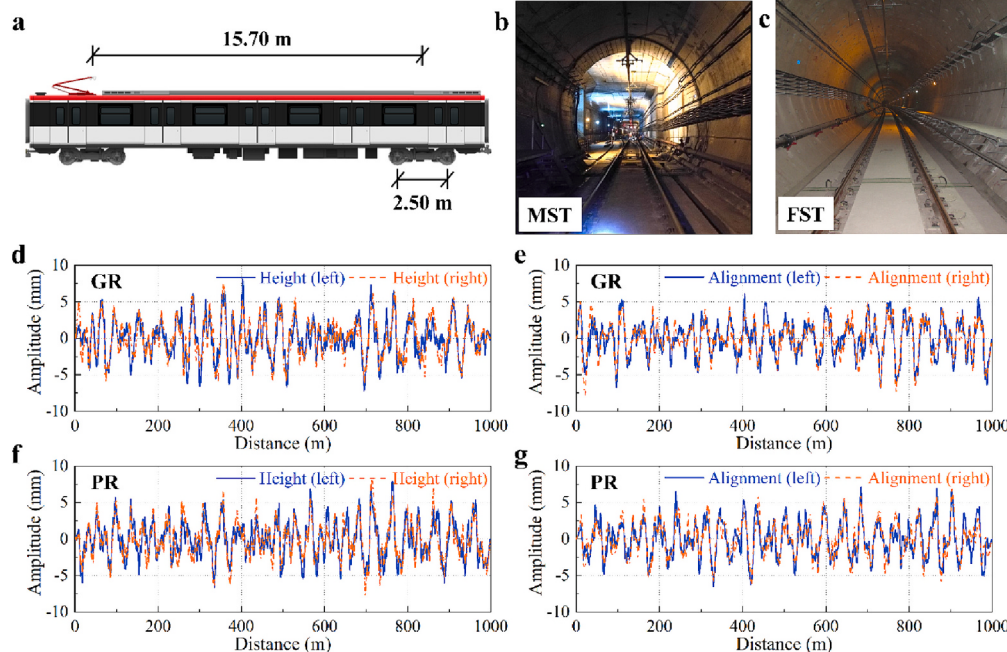


**Fig. 5.** Illustration of the characteristics of the vehicle-track system: (a) characteristic length of the vehicle, (b) monolithic slab tracks (MST), (c) steel spring floating slab tracks (FST), (d) height irregularity under good track condition, (e) alignment irregularity under good track condition, (f) height irregularity under poor track condition and (g) alignment irregularity under poor track condition.

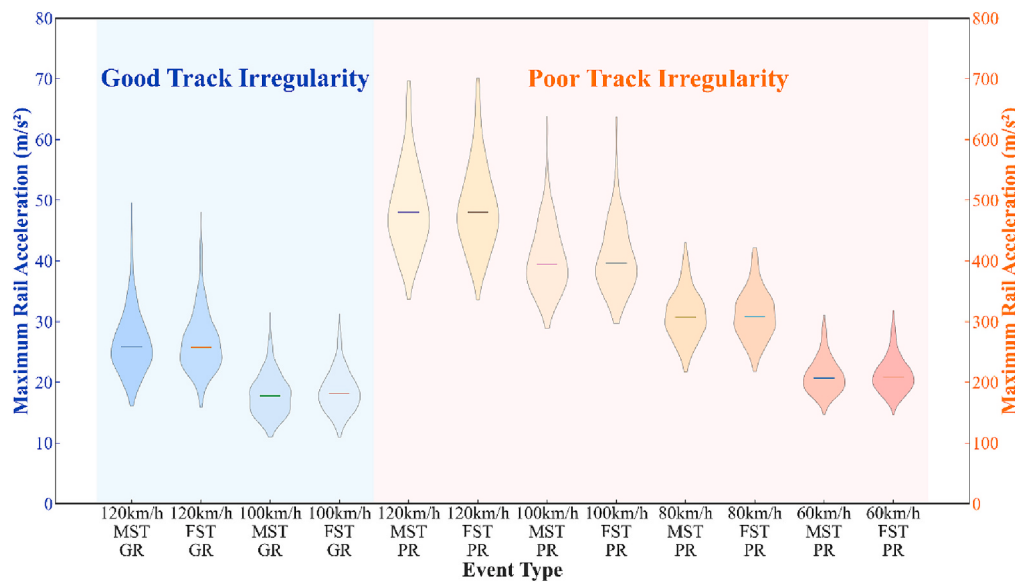


**Fig. 6.** Statistical analysis of peak vibration accelerations in the time domain.

signaling systems, turnout settings, and gradients to ensure train safety and on-time arrivals. Additionally, with the aid of advanced technologies such as Automatic Train Control (ATC), Automatic Train Protection (ATP), and Automatic Train Operation (ATO), trains can maintain approximately constant speeds in certain sections. Therefore, in the case study, four typical train speeds (120 km/h, 100 km/h, 80 km/h, 60 km/h) are considered to study their impacts on rail vibration characteristics and rail PEH performance. The characteristic length of the vehicle is depicted in Fig. 5(a). More detailed information about vehicle dynamics parameters can be found in **Table I** in **Appendix B**.

Track construction and dynamic properties significantly affect train operational conditions and performance, as well as rail vibration frequency characteristics. This study considers two typical types of subway tracks: monolithic slab tracks (MST) and steel spring floating slab tracks (FST). As shown in Fig. 5(b), MSTs consist of rails, fastening systems, subgrade, and foundations. With a smaller track structure unit and more robust foundation, MSTs can bear larger axle loads and offer higher vertical stiffness, thus effectively suppressing lateral and longitudinal vibrations and ensuring train stability. FSTs comprise rails, fastenings, concrete foundations, and intermediate steel springs. As depicted in Fig. 5(c), the steel springs provide high stiffness and durability to effectively reduce track noise & vibration and improve subway comfort and operational efficiency. Unlike MSTs, FSTs have softer lateral and longitudinal dynamic properties, resulting in more noticeable influences on the wheel-rail dynamic response. **Table II** in **Appendix B** lists the dynamic parameters associated with the two types of tracks.

The geometric state of tracks exhibits noticeable randomness due to various influencing factors, including rail initial bending, wear, damage, uneven sleeper spacing, inconsistent mass, uneven subgrade grading and strength, loosening, pollution, uneven settlement of plate-structure subgrade, and stiffness variations [1]. These factors collectively constitute the random characteristics of track irregularity. Various track irregularities found on actual lines result from the superposition of random irregular waves with different wavelengths, phases, and amplitudes, creating a complex random process related to track mileage. Generally, the power spectral density (PSD) function is the most important and commonly used statistical function to describe track irregularity as a stationary random process. The derived track spectrum can clearly display the relationship between irregularity magnitude and frequency. However, in the nonlinear vehicle-track coupled dynamic model employed in this study, system excitation uses a time-domain input to facilitate numerical solving. Therefore, it is necessary to

convert the track random irregularity PSD function into space-domain samples of track irregularity that vary with track mileage. An algorithm based on equivalent frequency-domain power spectra is employed for this conversion [1]. First, the amplitude and random phase of the track spectrum are determined from the track random irregularity PSD. Then, the inverse Fourier transform (IFFT) is used to obtain time-domain simulation samples of track irregularity. The American Class 6 track irregularity spectrum is adopted to replicate the general state of railway track, with a considered wavelength range spanning from 0.5 m to 50 m. Based on this, this study incorporates short-wave irregularities measured on railways to create two composite track geometry irregularity states:

- The first composite state incorporates the American Class 6 track irregularity spectrum along with short-wave components ranging from 0.05 m to 0.99 m, corresponding to the GR condition in **Table 2**. The space-domain samples of track irregularity converted from the combined frequency-domain PSD are illustrated in Figs. 5(d) and (e), depicting the height and alignment irregularities of the track, respectively.
- The second composite state introduces short-wave components ranging from 0.01 m to 0.99 m into the American Class 6 track irregularity spectrum, corresponding to the PR condition in **Table 2**. The converted composite track irregularity space-domain samples are depicted in Figs. 5(f) and (g), which showcase the height and alignment irregularities of the track, respectively, after the amalgamation of these components.

#### 4.2. Rail excitations in different scenarios

Existing research on rail vibration energy harvesting typically focuses on the PEH design based on data from a specific location on the rail under a particular operating condition. Alternatively, most of those studies involve excessive model simplification of the vehicle-track system. In those works, the dominant frequency of rail vibration can be clearly distinguished in the spectrum, enabling the easy alignment of the PEH natural frequency with the rail's principal frequency. However, this method overlooks the variability and complexity of the track vibration spectrum in real train operation scenarios. Based on the vehicle-track spatial coupled dynamic model established in Section 3.2, this paper calculates the vibration acceleration data of the rail under 3600 operating conditions (each rail vibration acceleration data is defined as an

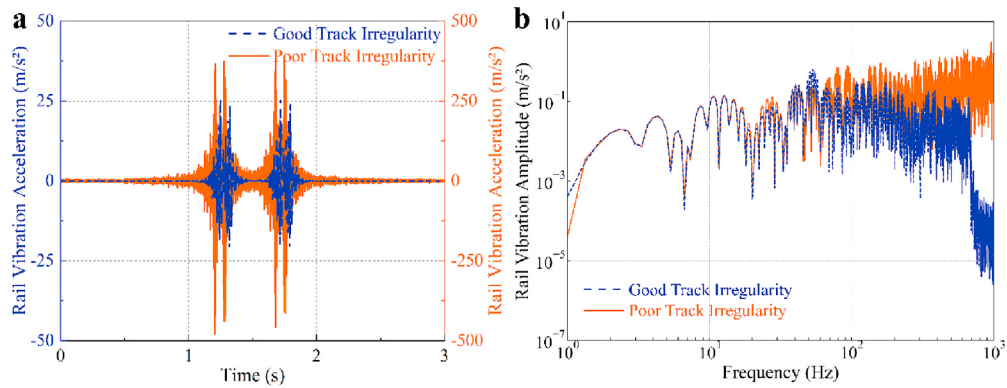


**Fig. 7.** Typical rail vibration responses in the (a) time and (b) frequency domain.

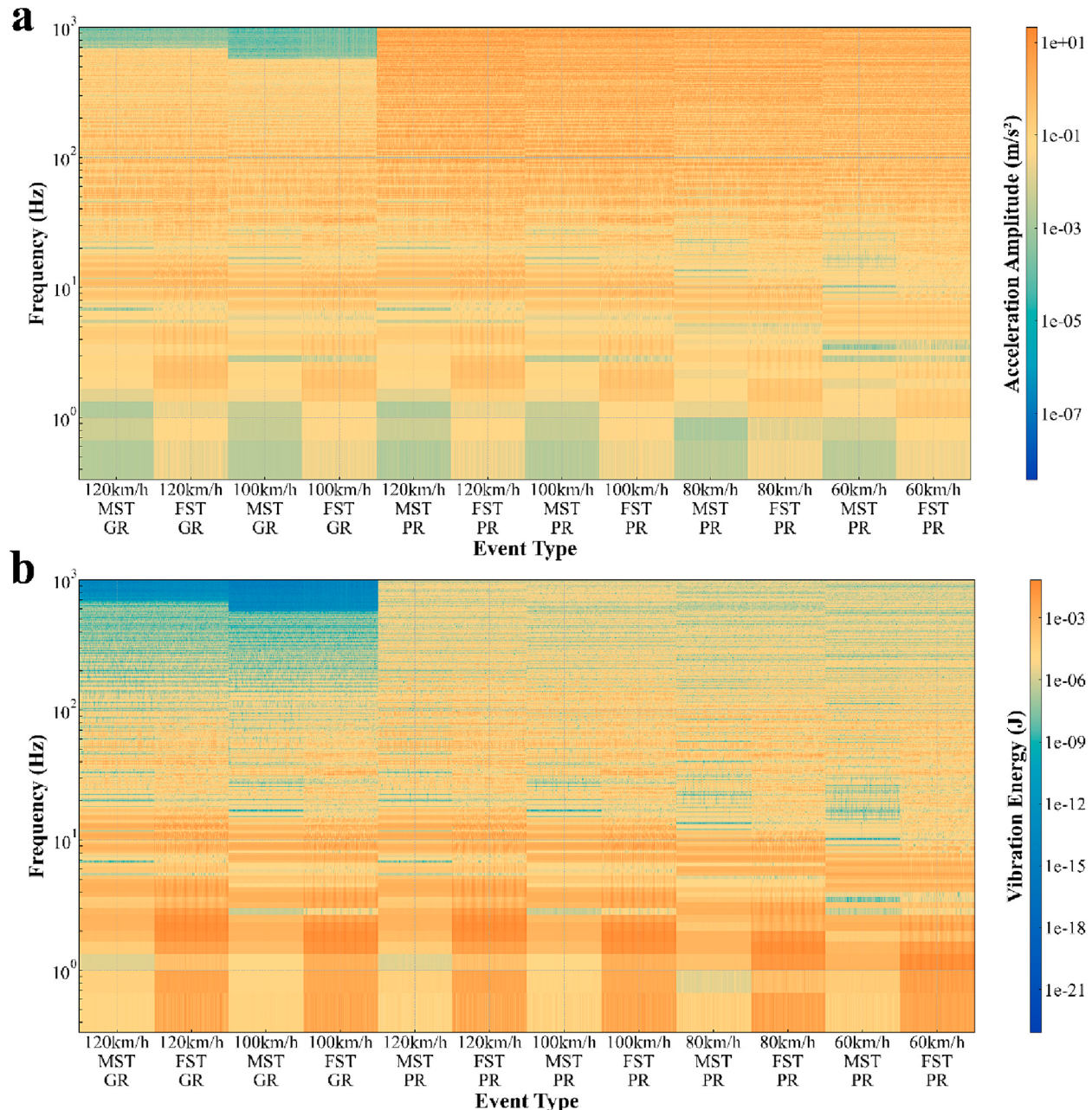


**Fig. 8.** Frequency-domain statistical analysis of rail vibration datasets from perspectives of (a) amplitude and (b) vibrational energy.

'event' in this work). These calculations are to thoroughly investigate the impacts of train speed, track structure types, and track geometry irregularity wavelength on the rail vibration frequency and the PEH performance. Prior to optimizing the PEH, it is essential to analyze the characteristics of rail vibration, which is the input excitation for the PEH, and to understand the characteristics under different operating conditions.

**Fig. 6** provides a statistical analysis of 12 types of rail vibration data in the database, depicted as violin plots, from the perspective of peak vibration values in the time domain. Within each violin plot in **Fig. 6**, the width signifies data density, indicating more data points where it is broad and fewer where it is narrow. A horizontal line within each violin represents the median of the data. The four data sets with a blue background correspond to the four conditions with better track smoothness. The peak values are to read from the blue Y-axis on the left. The eight data sets with a pink background correspond to eight conditions with worse track smoothness. The vibration peak values are to read from the orange Y-axis on the right. From the speed perspective, regardless of the type of track or track smoothness, the rail vibration acceleration increases as the train speed increases. For instance, when speed increases from 60 km/h to 120 km/h on a FST under poor smoothness, the average vibration acceleration increases from 212.26 m/s<sup>2</sup> to 488.82 m/s<sup>2</sup>, more than doubling in value. Considering the type of track, no significant difference in vibration acceleration is noted between the FST and the MST across all speed levels. For example, given the vehicle speed is 100 km/h, the average vibration acceleration for the FST is 184.67 m/s<sup>2</sup>, while the MST is 179.50 m/s<sup>2</sup>, exhibiting a pretty minor difference. Regarding track smoothness, for the same type of track and speed level, the vibration acceleration of tracks with poor smoothness (PR) is generally higher than that of tracks with good smoothness (GR). For example, at a speed of 120 km/h for a FST, the average vibration acceleration for the PR track is 488.82 m/s<sup>2</sup>, while the GR one is 265.42 m/s<sup>2</sup>. The difference is remarkably large.

**Fig. 7** presents the time-history and frequency-domain curves of the rail vibration data for two typical events. It is noteworthy that the two typical sets of rail vibration data shown in **Fig. 7(a)** and (b), respectively, correspond to the median amplitude data under two types of conditions at a speed of 120 km/h and MST conditions. The unevenness of the track significantly affects the rail vibration amplitude. Thus, a double Y-axis graph (**Fig. 7(a)**) is used to plot the rail vibration acceleration time series curve. The blue curve represents the rail vibration acceleration with better track smoothness. Its amplitude is to be read from the blue coordinate axis on the left. Compared to the rail vibration acceleration data for poor track smoothness (the orange curve), the maximum amplitude of the former case is 25.83 m/s<sup>2</sup>, which is significantly smaller than that of the latter, 479.37 m/s<sup>2</sup>. The logarithmic frequency spectrum curve plotted in **Fig. 7(b)** shows that the two data sets have similar vibration amplitudes within the low frequency of 80 Hz. However, when the frequency is higher, the rail vibration amplitude under poor track smoothness is significantly higher than that under good track smoothness. This is because the shorter track unevenness induces more severe wheel-rail interactions. In addition, it can be observed that the spectrum data corresponding to the blue color significantly decreases after 666.67 Hz. This is because the shortest wavelength of track unevenness is limited to 0.05 m. Given a vehicle speed of 120 km/h, a rough calculation by  $f = v/l$  tells that the track unevenness cannot stimulate higher-frequency rail vibration.

Understanding the excitation frequency distribution can help better design the geometric parameters of the PEH. Using Fourier transforms, the time-history rail vibration acceleration data can be converted to the frequency domain, as shown in **Fig. 8(a)**. Data in the database are divided into 12 types, each containing 300 sets of data. From the figure, we can observe that the amplitude in the high-frequency area of the spectrum corresponding to the first four event types is very small. This is because the smallest track irregularity wavelength used in the simulation is 0.05 m, which cannot stimulate higher frequency vibrations. In

contrast, the data corresponding to the other eight event types within a shorter wavelength range have more energy concentrated in the high-frequency range. The floating slab track has richer frequency domain components in the low-frequency area for the same train running speed and track smoothness. However, during the actual vibration energy harvesting process, the mass does not "like" to shake at high oscillation frequencies, and the mass impedance increases with frequency. Therefore, before designing PEH, it is necessary to understand the vibration energy distribution in the frequency domain.

By substituting Hooke's law for  $k$  ( $k = F/x$ ) and Newton's second law for  $F$  ( $F = ma$ ), and converting from displacement to acceleration ( $x = ca/f^2$ ), where  $c$  is a constant for conversion, we can find the total energy of vibration [72],

$$E_{Total} = c \frac{ma^2}{2f^2} \quad (13)$$

where  $c = 1$  if using SI units,  $m$  = Mass in kg (total mass of the vibrating object, in this section  $m = 1$ , to calculate the rail vibration energy per unit mass),  $a$  is the rail vibration acceleration in m/s<sup>2</sup>, and  $f$  is the frequency in Hz. The distribution of calculated rail vibration energy is shown in **Fig. 8(b)**. The vibration energy of each data group mainly concentrates in the low-frequency area below 100 Hz, which underscores the importance of low-frequency vibration energy harvesting. Similarly, it can also be observed that the rail has very little high-frequency vibration when the track is in a good state, and the data corresponding to the FST concentrates more in the low-frequency area. These phenomena are consistent with **Fig. 8(a)**.

By incorporating the complexities of train speed, track type, and track irregularity, this study provides a more comprehensive understanding of rail vibration characteristics and their effects on PEH performance. Consequently, this research will enable the development of more effective PEH designs that better account for the variability and complexity of real-world train operation scenarios, ultimately improving energy harvesting capabilities.

Furthermore, our analysis of rail vibration excitations reveals that peak accelerations can reach as high as 700 m/s<sup>2</sup> under poor rail conditions. To ensure that the optimized PEH operates within the safe regime, a comprehensive safety verification was conducted for each excitation event during the optimization process. For demonstrative purposes in the work, we specifically focused on the scenario exhibiting the highest peak acceleration within the rail vibration database. The optimized PEH configuration for this extreme case was established with the following parameters:  $L_s = 0.058303$  m,  $l = 0.793816$ ,  $h = 0.968910$ ,  $b_s = 0.006106$ ,  $w = 0.966345$ , and  $M_t = 0.013970$  kg. This particular scenario, with a peak acceleration of 700.986 m/s<sup>2</sup> and a RMS acceleration of 38.926 m/s<sup>2</sup>, served as a critical test case. Our detailed stress and strain analysis, especially at the root of the PEH where maximum stress and strain are typically observed, validated the structural integrity of the design. The simulation results indicated that the maximum stress at the root reached 158.84 MPa with a corresponding peak strain of  $4.82 \times 10^{-4}$ , well below 60% of the material ultimate limits. Additionally, the maximum displacement observed at the free end of the beam was 7.31 mm under these high-intensity excitations, confirming the safety and robustness of the PEH in operation. These findings not only demonstrate the resilience of our model against high-impact events but also underscore the reliability of our optimized PEH design in maintaining structural integrity under extreme operational conditions.

## 5. Results and performance evaluation

### 5.1. Cluster analysis results

The proposed event-driven optimization strategy aims to search for candidates to maximize the harvested energy and determine appropriate PEH parameters under different operating conditions by considering

**Table 3**

Properties of cantilever substrate, piezoelectric transducer.

Properties	Cantilever substrate	Piezoelectric element
Material	Copper	MFC M2814-P2
Length (mm)	To be optimized	To be optimized
Width (mm)	To be optimized	To be optimized
Thickness (mm)	To be optimized	0.3
Mass density ( $\text{kg}/\text{m}^3$ )	8960	5440
Young's modulus (GPa)	110	30.336
Permittivity ( $\text{F}/\text{m}$ )	–	$1.3281 \times 10^{-8}$
Piezoelectric constant ( $\text{pm}/\text{V}$ )	–	-170

various characteristics of the subway lines. In [Section 4](#), we have considered 12 types of track conditions, amounting to 3600 events, as representative data to characterize the vibration features of the rail in different scenarios and under different conditions. We used six design parameters to characterize the PEH geometry: substrate length  $L_s \in [58, 100]$  mm, the dimensionless piezoelectric layer length  $l \in [0.4, 1]$ , the dimensionless piezoelectric layer thickness  $h \in [0.3, 1]$ , the substrate width  $b_s \in [4, 20]$  mm, the dimensionless piezoelectric layer width  $w \in [0.4, 1]$ , and the concentrated mass at the free end of the piezoelectric cantilever beam  $M_t \in [0, 10]$  g. Other parameters of the PEH are listed in [Table 3](#).

The optimization was performed separately for the 3600 events using

the PSO algorithm. We determined the optimal parameters of the PEH that can maximize the output energy density in each event. As a result, 3600 optimal geometries were obtained. It should be noted that the optimal resistance in each event is different during the optimization processes. The optimization problem involves 6 design variables, and the energy density is the figure of merit we use to evaluate the performance of the PEHs. Therefore, we plotted the  $7 \times 7$  subplots, as shown in [Fig. 9](#), to help better understand the distribution of the obtained optimal PEH parameters and their corresponding energy densities. The nuclear density scatter plots in the upper off-diagonal of [Fig. 9](#) demonstrate the two-dimensional distribution of any two variable combinations, where the area in deeper orange indicates denser distribution. The curves on the main diagonal describe the distribution of each variable within the value space. The contour heat maps in the lower off-diagonal describe the probability density distribution, with deeper colors indicating higher probability densities. The circles and ellipses indicate the shape of the data distribution in the two-variable space. The more compact the circle or ellipse, the stronger the correlation between the two variables. The major axis direction of the ellipse indicates the direction of correlation between the variables. A horizontal/vertical ellipse indicates a weak correlation; an oblique ellipse indicates a positive/negative correlation. These graphs can help us understand the relationship between two variables and the data distribution within these two variable spaces.

From the curves on the main diagonal of [Fig. 9](#), we can see that after

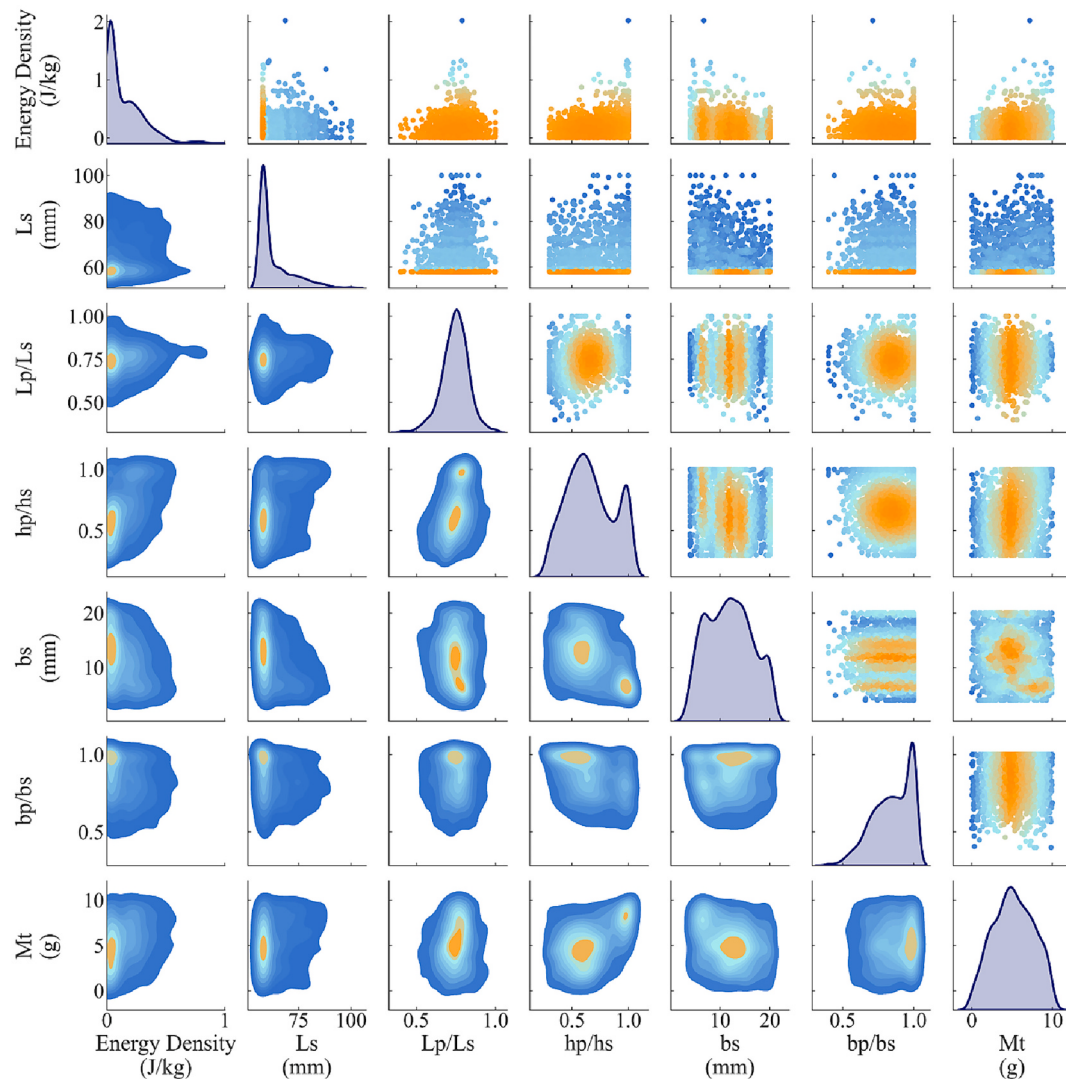


**Fig. 9.** Optimal PEH geometries for 3600 events in the rail vibration dataset.

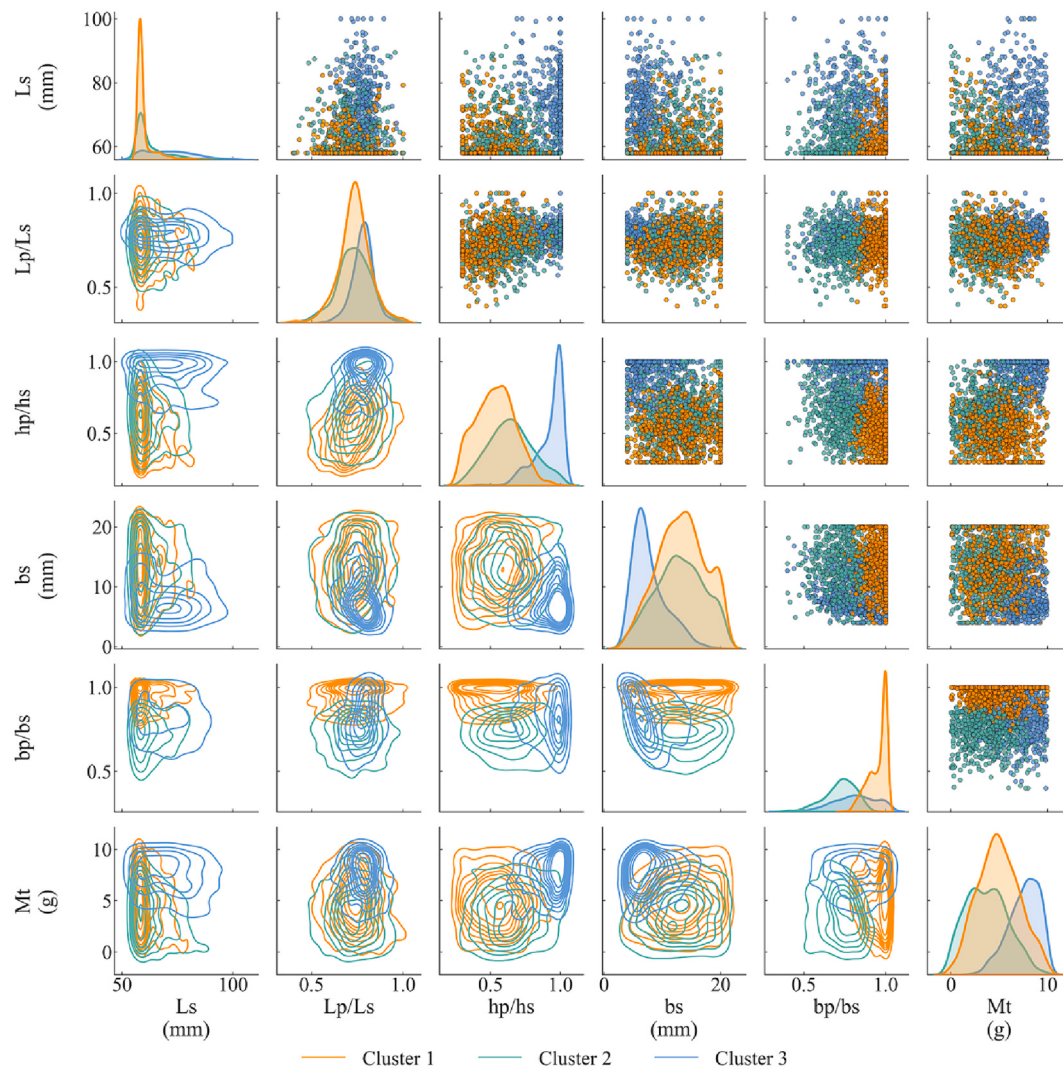


**Fig. 10.** Multivariate distribution and correlation analysis with clustering in parameter space.

PSO optimization, the variables primarily converged to some intermediate values in their design spaces. The subplot (2,2) of Fig. 9 shows the distribution of the substrate beam length after optimization. The substrate beam length tends to take values near the lower limit of the design space. The subplot (3,3) demonstrates the optimized piezoelectric coverage ratio by the PSO algorithm. According to the PSO algorithm, covering the entire substrate beam with piezoelectric materials is unnecessary. This is because stresses in the piezoelectric cantilever beam mainly concentrate at the clamped root, and covering the segment near the free end is not cost-effective. Similarly, subplots (4,4) and (5,5) demonstrate the optimized dimensionless piezoelectric layer thickness and the substrate beam width. The optimal values are obtained at the intermediate, and the multiple peaks on the curve indicate the existence of local optimum. The subplot (6,6) shows the optimized dimensionless piezoelectric layer width by the PSO algorithm. The optimized dimensionless piezoelectric layer width is almost 1 in most events, indicating that the larger the coverage rate of the piezoelectric layer in the width direction, the better the energy harvesting performance. Finally, it is worth noting that in the subplot (7,7), the optimized concentrated mass does not exhibit a significant positive correlation with the objective function. However, the optimal value falls in the middle of the design interval.

Using the K-Means method, we grouped the 3600 sets of optimal solutions for different events into clusters. Moreover, we used the

Silhouette Coefficient as the metric to measure the clustering goodness. It offers insights into how well the data were clustered and the performance of the clustering model even in the absence of labels. By calculating the Silhouette Coefficient, the optimal  $k$  value was found to be 3, which suggests grouping the data into 3 clusters. Similarly, a matrix diagram can be used to illustrate the distribution of the six optimized variables in the value space for each cluster after clustering analysis, as shown in Fig. 10. The sub-graphs on the primary diagonal line use orange, green, and blue curves to characterize the distribution of the optimized variables in the three clusters. The orange curve corresponding to the Cluster 1 distribution contains the most optimized cases, followed by green and blue curves representing Cluster 2 and 3 distributions. Recalling the peaks of the curves on the main diagonal in Fig. 9 and comparing them with the results in Fig. 10, we can understand that those peaks indicate different cluster features identified by the clustering analysis. The differences in the three distributions provide evidence for the effectiveness of clustering analysis.

The clustering analysis has divided the 3600 rail vibration events into three clusters. To identify the essential features of each cluster for guiding the design of the PEH under different operating conditions, it is necessary to first figure out how the excitation events are distributed. The bubble chart in Fig. 11 shows the distributions of the three clusters and the corresponding 12 excitation types. The bubble size indicates how many times the event occurs, i.e., the larger the bubble, the more

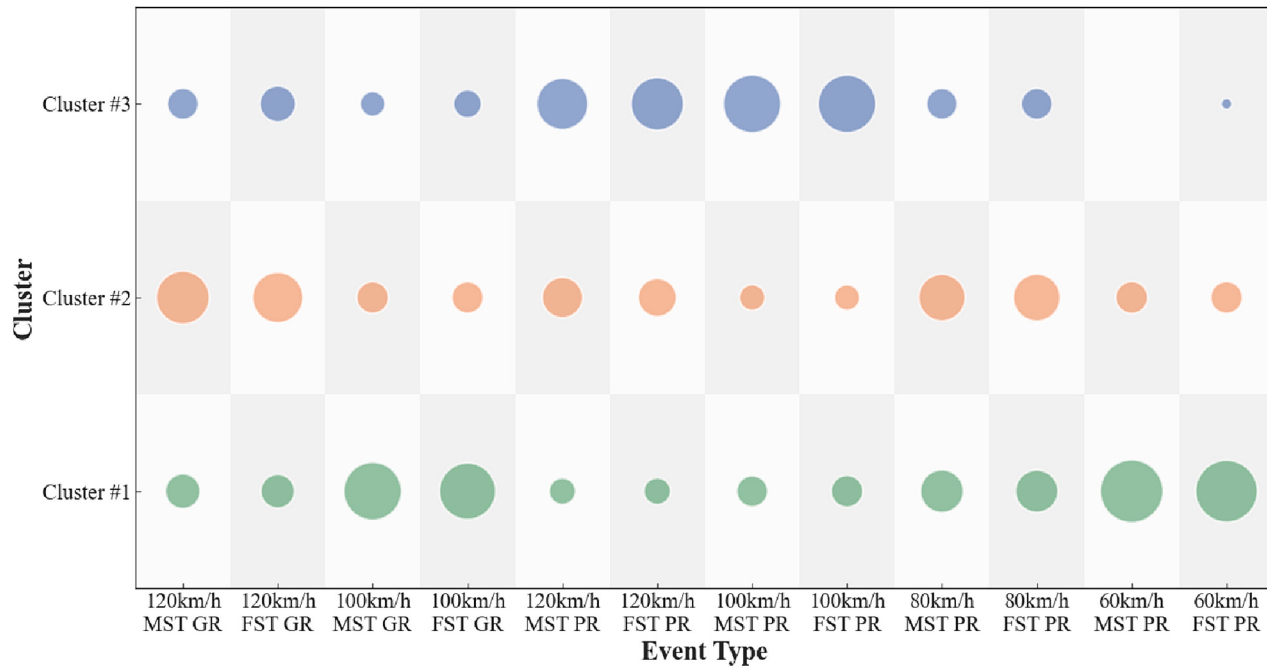


**Fig. 11.** The event distribution of different types in the clusters.

**Table 4**  
Geometry configurations of selected candidates.

Candidate	$L_s$ /mm	$l (L_p/L_s)$	$h (h_p/h_s)$	$b_s$ /mm	$w (b_p/b_s)$	$M_t$ /g
1	69.05	0.78	0.94	8.15	0.82	9.30
2	66.51	0.69	0.65	11.88	0.71	2.93
3	59.59	0.75	0.55	13.78	0.93	5.00

often the event occurs. The  $x$ -axis represents different excitation types, and the  $y$ -axis represents different clusters. Thus, it is clear that the events with good track smoothness and lower vehicle operating speeds mainly drop into Cluster 1. In Cluster 2, the distributions of the 12 event types are relatively uniform. In comparison, events with poor track smoothness and higher speeds are relatively less common in this cluster. In contrast, the cases of Cluster 3 are mainly events with poor track smoothness and higher vehicle operating speeds. A notable observation is the absence of events in Cluster #3 for the “60km/h MST PR” condition. Likewise, Cluster #3 displayed a scarcity of events for the “60km/h FST PR” condition. These findings strongly suggest that Clusters #1 and #2 outperform Cluster #3 substantially when it comes to these particular conditions. Given the frequency domain analysis of the rail vibration excitation in **Figs. 8(a) and (b)**, the clustering analysis results can be understood as the differences in rail vibration energy distribution caused by the train operating speeds and the irregularities of the track. The PEH optimization design is to maximize the output energy density by tuning its natural frequency. Therefore, the differences in the frequency spectra of the excitation events directly affect the clustering analysis results.

## 5.2. Performance evaluation and validation

In practice, we expect to have several representative PEHs that can deal with most events in different clusters. On the other hand, it is almost infeasible to design one PEH for each event or perform an optimization study in long-time windows due to limited computational resources. To overcome this limitation, in this section, we choose the design at the centroid of each cluster as the representative to tackle the events in that cluster. In the studies of this work, the respective centroids corresponding to the 3 clusters are listed in **Table 4**.

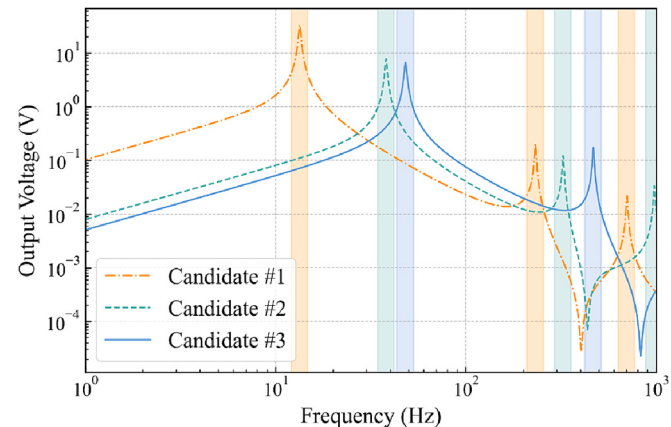


**Fig. 12.** Voltage FRF of the three PEH candidates.

The three representative candidates are tested under the basic excitation of  $1 \text{ m/s}^2$ , and their corresponding voltage FRF responses are shown in **Fig. 12**. The resonant frequencies of the three representative candidates are highlighted by color blocks. The electrical resistances are swept, and the optimal one that maximizes the FRF peak at the fundamental resonant frequency is used. Specifically, the optimal resistances for these three candidates are 628, 215, and  $118\text{k}\Omega$ , respectively. As shown in **Fig. 12**, Candidate #1 and #2 have three resonant frequencies below 1000 Hz. The first three resonant frequencies of Candidate #1 are 13.39, 231.76, and 701.96 Hz, and those of Candidate #2 are 38.05, 324.34, and 977.28 Hz. Candidate 3 has only two resonant frequencies below 1000 Hz, which are 48.17 Hz and 467.68 Hz. The resonant frequencies of the three chosen candidates follow an ascending sequence in the expected pattern. Most excitation events in Cluster #1, including Candidate #1, are with good track smoothness or lower train operating speeds. Thus, the corresponding rail vibration excitation frequencies are relatively low. Conversely, the rail vibration excitation frequency in the event of Candidate #3 is relatively high due to the high train speed. Hence, the fundamental resonant frequency of the optimized PEH is accordingly high.

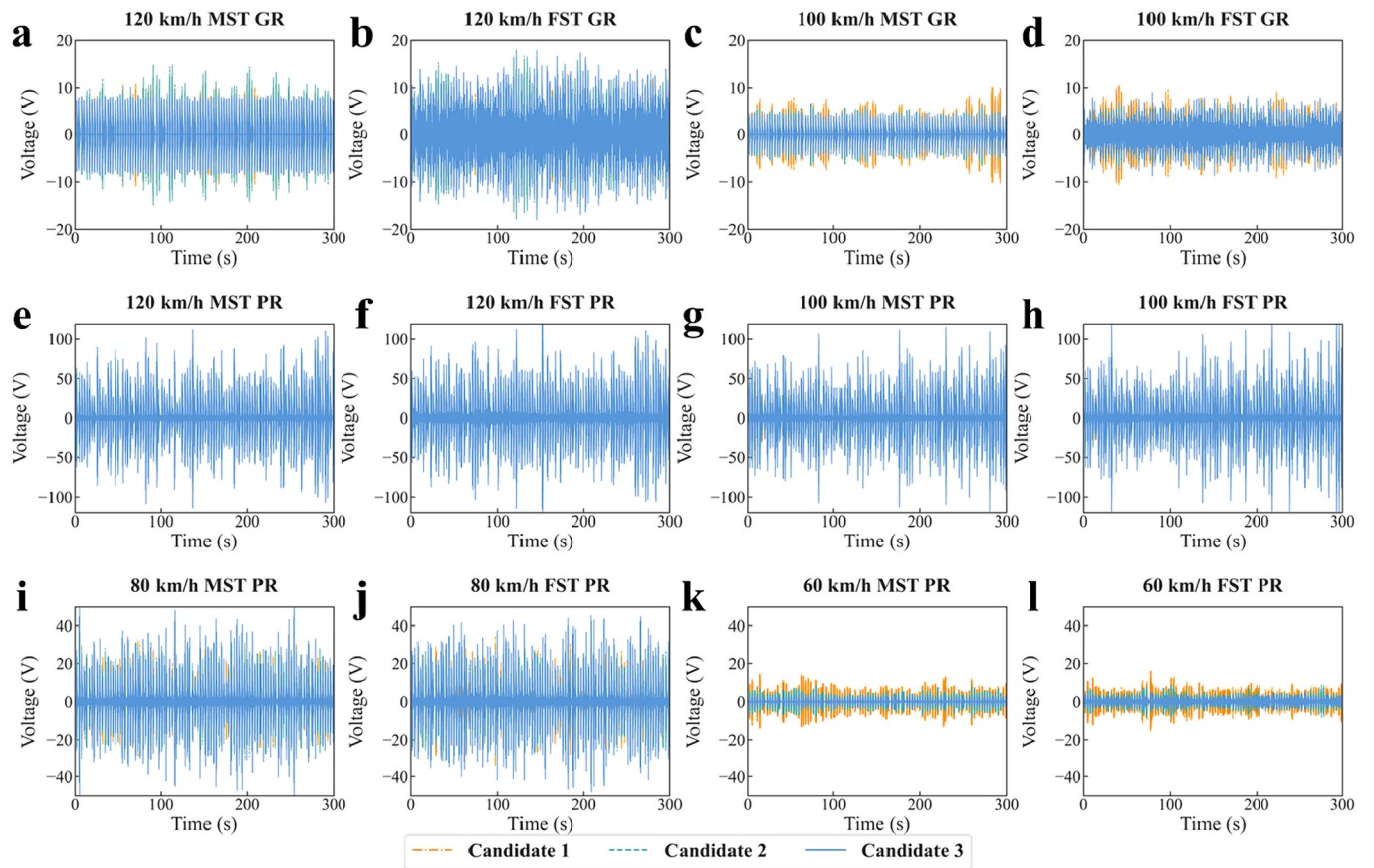


**Fig. 13.** Time-history voltage outputs of selected candidates in continuous energy generation.

**Table 5**  
Root mean square output voltage across diverse event types (Unit: V).

Event type	120 km/ h MST GR	120 km/ h FST GR	100 km/h MST GR	100 km/h FST GR	120 km/ h MST PR	120 km/ h FST PR
Candidate #1	1.235	1.623	1.131	1.545	4.110	4.352
Candidate #2	2.112	2.723	0.711	0.976	7.129	6.990
Candidate #3	2.728	4.280	1.164	1.874	19.937	21.362
Event type	100 km/ h MST PR	100 km/ h FST PR	80 km/ h MST PR	80 km/ h FST PR	60 km/h MST PR	60 km/h FST PR
Candidate #1	4.067	4.416	3.895	3.865	1.855	1.996
Candidate #2	3.807	3.971	4.757	4.803	1.051	1.158
Candidate #3	18.820	20.020	6.934	7.040	0.542	0.861

The three representative candidates are tested using twelve groups of validation data sets, which corresponded to the twelve types of events in [Section 4](#). Each validation data set contains 100 rail vibration acceleration data. The time-history voltage outputs of the three PEHs are shown in [Fig. 13](#). Moreover, the RMS voltage and power outputs of the three candidates are summarized in [Tables 5–6](#). As shown in [Fig. 13\(a\)-\(d\)](#), the three candidates have remarkably large voltage outputs under the four conditions with good track irregularities. It can be seen that the voltage output corresponding to the condition with a speed of 120 km/h is significantly larger than the one corresponding to 100 km/h. When the train runs at 120 km/h on a monolithic slab track with a good track

**Table 6**  
Root mean square output power across diverse event types (Unit: mW).

Event type	120 km/h MST GR	120 km/h FST GR	100 km/h MST GR	100 km/h FST GR	120 km/h MST PR	120 km/h FST PR
Candidate #1	0.013	0.022	0.011	0.02	0.144	0.161
Candidate #2	0.038	0.063	0.004	0.008	0.432	0.415
Candidate #3	0.063	0.156	0.012	0.03	3.378	3.878
Event type	100 km/h MST PR	100 km/h FST PR	80 km/ h MST PR	80 km/ h FST PR	60 km/ h MST PR	60 km/ h FST PR
Candidate #1	0.141	0.166	0.129	0.127	0.029	0.034
Candidate #2	0.123	0.134	0.192	0.196	0.009	0.011
Candidate #3	3.01	3.406	0.409	0.421	0.002	0.006

irregularity condition, the transient peak voltage of Candidate #2 reaches a maximum of 15.19 V, followed by Candidate #1 with a peak voltage of 12.34 V. The maximum peak voltage of Candidate #3 is only 8.90 V. When the train runs at the same speed on a floating slab track with good track smoothness, the voltage performance of the three PEHs is similar to that on the monolithic slab track. However, when the train speed decreases to 100 km/h, Candidate #1 achieves the maximum transient voltage output, as shown in [Fig. 13\(c\)-\(d\)](#). [Fig. 13\(e\)-\(h\)](#) show the voltage outputs of the three PEHs when the track irregularity is poor and the vehicle speed is high. Due to the significant increase in the excitation amplitude, the voltage outputs of the three PEHs are

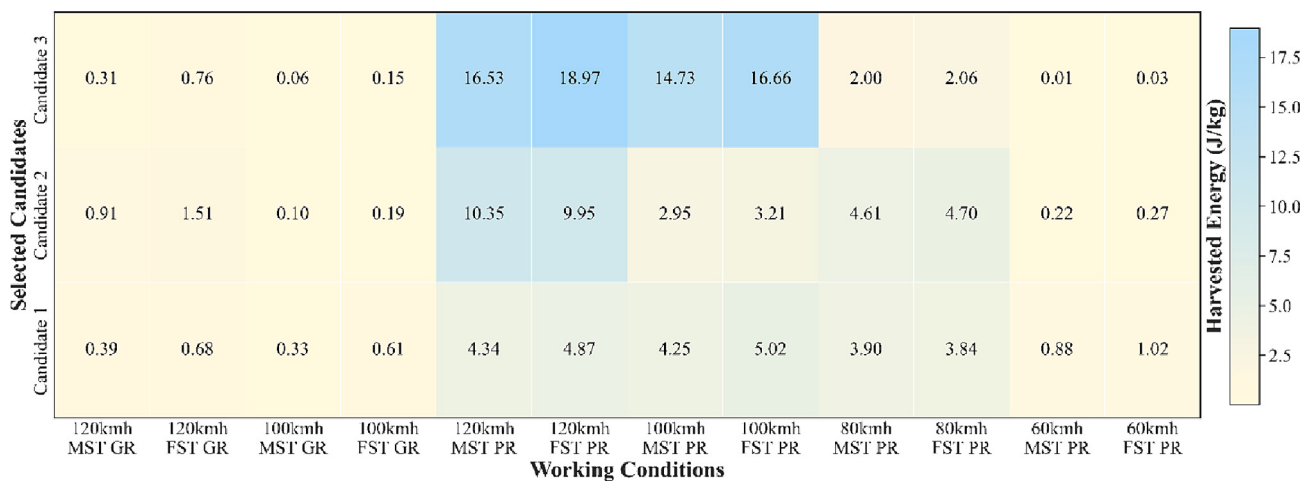


**Fig. 14.** Energy densities of the three representative candidates at different working conditions.

significantly increased compared to the previous four. When the train speed is 120 km/h on a monolithic slab track with poor track smoothness, the peak voltage output of Candidate #3 reaches a maximum of 114.22 V, followed by Candidate #2 with a peak voltage of 68.59 V. The peak voltage of Candidate #1 is the smallest, only 44.81 V. In other words, the peak output voltage of Candidate #3 is 154.90% larger than that of Candidate #1. The same phenomenon is observed in Fig. 13(f)-(h). The tendencies shown in Fig. 13(i)-(l) are similar to those in Fig. 13(a)-(d), and therefore are not repeated here. The above analysis shows that the energy harvesting performance of the three differently configured PEHs for tackling different conditions is incredibly different. It is, thus, proved that properly configuring the PEH is crucial for railway vibration energy harvesting.

The energy densities of the three candidates under different excitation types are shown in Fig. 14. The three PEHs show advantages under different conditions. When the train speed is 120 km/h on a track with good irregularity, Candidate #2 generates a higher energy density than the other two candidates under all these conditions. Specifically, under the condition of 120 km/h on a floating slab track, its energy density (1.51 J/kg) far exceeds Candidate #1 (0.68 J/kg) and Candidate #3 (0.76 J/kg), which indicates that Candidate #2 is more sensitive to conditions with high speed and good track smoothness. When the track irregularity is poor, the energy density produced by Candidate #3 significantly increases on monolithic slab tracks and floating slab tracks at high speeds (120 km/h and 100 km/h), exceeding the other two candidates. Particularly under the condition of 120 km/h on a floating slab track, the energy density of Candidate #3 (18.97 J/kg) is much higher than Candidate #1 (4.87 J/kg) and #2 (9.95 J/kg). This implies that Candidate #3 has stronger adaptability to poor track smoothness and high-speed conditions. At low train speeds (80 km/h and 60 km/h) on monolithic and floating slab tracks, the energy densities of all three candidates decrease. The decreases for Candidates #1 and #2 are smaller, and their energy densities are still relatively high. This manifests that Candidates #1 and #2 perform better in collecting vibration energy under low-speed conditions. In summary, these results reveal the performance characteristics of different PEHs under different conditions, providing important information for us to understand and optimize the design of PEHs.

## 6. Conclusions

In this work, we proposed an event-driven approach to address the challenges of enhancing the energy harvesting performance of PEHs in the context of railway track vibration scenarios. To achieve this, we first utilized a distributed parameter model for partially covered PEHs based on the Euler-Bernoulli beam theory. Then, we employed an advanced

vehicle-track coupled dynamic model to simulate the variability and complexity of track vibrations under various real-world conditions, encompassing different train speeds, track structure types, and track geometry irregularities. Moreover, we introduced a novel event-driven enhancement method, wherein we sought optimal PEH designs for a large number of specific vehicle-track simulation datasets, each representing a unique operational condition. Subsequently, we grouped these events based on their similarities and selected the centroid design for each cluster as the recommended solution to address events within that cluster. This streamlined approach significantly reduced the complexity of design optimization efforts when dealing with intricate and ever-changing scenarios. Notably, this research marks the pioneering introduction of an advanced vehicle-track coupled model into the realm of PEH design for railway applications.

Our study underscores several pivotal observations in the realm of piezoelectric energy harvesters for railway tracks:

- (1) Train speed, track type, and irregularities have a substantial impact on the characteristics of rail vibration. The distribution of short-wave components in track unevenness plays a significant role in shaping the rail vibration spectrum. The intricate nature of the rail vibration spectrum indicates that designing PEH cannot rely solely on simple frequency tuning.
- (2) Using collected energy density as the objective function in optimization aligns more closely with actual application scenarios. Despite the complexity of the rail vibration spectra in different conditions, the majority of rail vibration energy is concentrated within the 100 Hz range. As a result, when optimizing PEHs, particular attention should be given to their frequency characteristics in the low-frequency range.
- (3) Cluster analysis methods have been proven effective in classifying optimized variable combinations based on the distinctive attributes of rail vibration events. By retracing the event conditions corresponding to each cluster, we can gain a deeper understanding of the underlying rationale of cluster analysis. Moreover, the selection of cluster centroids allows for the rapid identification of a limited set of candidate solutions, facilitating the effective handling of most events.
- (4) The energy harvesting performance of various PEHs under different conditions can exhibit significant variations. In the case studies conducted, the energy density produced by three PEH configurations differed by up to 389.53%. Therefore, the selection of an appropriate PEH configuration is of paramount importance in the context of railway vibration energy harvesting.

Overall, the enhancement method proposed in this work signifies a

versatile solution for harnessing energy across a spectrum of railway vibrations. The inherent adaptability of the strategy suggests its potential to account for challenges arising from curved tracks, varied track gradients, different speed profiles, and changes in vehicle suspension systems. This approach shows promise especially in scenarios characterized by discrete vehicle and track parameters. While the current study focuses on rectangular geometries with constant thickness, foundational principles of the method afford it the latitude to accommodate more intricate design. Further refinements can be achieved by integrating alternative modeling techniques, such as the finite element method and the Timoshenko beam-based models, enhancing the modeling accuracy. Additionally, both the cluster analysis method and the optimization algorithm employed here can be substituted as needed to suit the specific requirements of different applications. The flexibility of the proposed method paves the way for tailored adaptations in distinct applications, cementing the roadmap for future innovations in energy harvesting.

#### CRediT authorship contribution statement

**Shuai Qu:** Writing – review & editing, Writing – original draft, Visualization, Validation, Software, Methodology, Investigation, Formal analysis, Conceptualization. **Yuhao Ren:** Software, Data curation. **Guobiao Hu:** Writing – review & editing, Validation, Methodology,

#### Appendix A. Vehicle-track coupled dynamic model

The detailed expressions of Eq. (11) are as follows:

$$\mathbf{M}_v = \text{diag}[M_c \ M_{t1} \ M_{t2} \ M_{w1} \ M_{w2} \ M_{w3} \ M_{w4}] \quad (\text{A1})$$

$$\mathbf{M}_{(\cdot)} = \text{diag}[m_{(\cdot)} \ m_{(\cdot)} \ m_{(\cdot)} \ I_{(\cdot)x} \ I_{(\cdot)y} \ I_{(\cdot)z}] \quad (\text{A2})$$

$$\mathbf{X}_v = \text{diag}[U_c \ U_{t1} \ U_{t2} \ U_{w1} \ U_{w2} \ U_{w3} \ U_{w4}] \quad (\text{A3})$$

$$\mathbf{U}_{(\cdot)} = \text{diag}[x_{(\cdot)} \ y_{(\cdot)} \ z_{(\cdot)} \ \phi_{(\cdot)} \ \beta_{(\cdot)} \ \psi_{(\cdot)}] \quad (\text{A4})$$

$$\mathbf{F}_v = [F_{vc} \ F_{vt1} \ F_{vt2} \ F_{vw1} \ F_{vw2} \ F_{vw3} \ F_{vw4}]^T \quad (\text{A5})$$

$$F_{vc} = \left[ \begin{array}{l} F_{(F-B)cx} - \sum_{i=1}^2 (F_{(L+R)2xi} + F_{(L+R)ksi}) \\ F_{(F-B)cy} + \sum_{i=1}^2 F_{(L+R)2syi} \\ F_{(F-B)cz} - \sum_{i=1}^2 F_{(L+R)2sz} + m_c g \\ d_s \sum_{i=1}^2 F_{(L-R)2sz} - H_{cb} \sum_{i=1}^2 F_{(L+R)2sy} \\ l_c \sum_{i=1}^2 (-1)^{i-1} F_{(L+R)2sz} - H_{cb} \sum_{i=1}^2 (F_{(R+L)2xi} + F_{(R+L)ksi}) \\ l_c \sum_{i=1}^2 (-1)^{i-1} F_{(L+R)2sy} + d_s \sum_{i=1}^2 F_{(R-L)2xi} + d_{sc} \sum_{i=1}^2 F_{(R-L)ksi} \end{array} \right] \quad (\text{A6})$$

$$F_{vui} = \left[ \begin{array}{l} F_{(L+R)2sxi} + F_{(L+R)xsi} - \sum_{k=2i-1}^{2i} F_{(L+R)1sxi} \\ -F_{(L+R)2syi} + \sum_{k=2i-1}^{2i} F_{(L+R)1syi} \\ F_{(L+R)2szi} - \sum_{k=2i-1}^{2i} F_{(L+R)1szi} + m_t g \\ -H_{tw} \sum_{k=2i-1}^{2i} F_{(L+R)1syi} + d_w \sum_{k=2i-1}^{2i} F_{(L-R)1szi} + d_s F_{(R-L)szi} - H_{bt} F_{(L+R)syi} \\ l_t \sum_{k=2i-1}^{2i} (-1)^{k-1} F_{(L+R)1szi} - H_{tw} \sum_{k=2i-1}^{2i} F_{(L+R)1sxi} - H_{bt} (F_{(L+R)2sxi} + F_{(L+R)sxi}) \\ l_t \sum_{k=2i-1}^{2i} (-1)^{k-1} F_{(L+R)1syi} + d_w \sum_{k=2i-1}^{2i} F_{(R-L)1sxi} + d_s F_{(L-R)2sxi} + d_{sc} F_{(L-R)sxi} \end{array} \right]_{(i=1 \sim 2)} \quad (A7)$$

$$F_{vwi} = \left[ \begin{array}{l} P_{(L+R)wx} + F_{(L+R)1sxi} \\ P_{(L+R)wy} - F_{(L+R)1syi} \\ -P_{(L+R)wz} + F_{(L+R)1szi} + m_w g \\ a_0 P_{(L-R)wzi} - r_{Li} P_{Lwzi} - r_{Ri} P_{Rwzi} + d_w F_{(L-R)1szi} + M_{(L+R)wx} + I_{wi} \dot{\psi}_{wi} (\dot{\beta}_{wi} - \Omega) \\ r_{Li} P_{Lwx} + r_{Ri} P_{Rwx} + a_0 \psi_{wi} P_{(L-R)wz} + M_{(L+R)wy} \\ a_0 P_{(L-R)wx} + a_0 \psi_{wi} P_{(L-R)wy} + d_w F_{(L-R)1sxi} + M_{(L+R)wz} + I_{wy} \dot{\phi}_{wi} (\dot{\beta}_{wi} - \Omega) \end{array} \right]_{(i=1 \sim 4)} \quad (A8)$$

For the components,  $M_c$ ,  $M_b$ , and  $M_w$  refer to the masses of the car body, bogie frame, and wheelset, respectively.  $I_{(\cdot)x}$ ,  $I_{(\cdot)y}$ , and  $I_{(\cdot)z}$  denote the inertia of the car body, bogie frame, or wheelset along the  $x$ ,  $y$ , and  $z$  axes.  $H_{cb}$ ,  $H_{bt}$ , and  $H_{tw}$  are the heights measured from the car body to the second suspension, from the car body to the bogie centroid, and from the bogie centroid to the wheelset centroid, respectively. They satisfy  $H_{cw} = H_{cb} + H_{bt} + H_{tw}$ . Semi-lateral distances for the first and second suspension and yaw dampers are given by  $d_w$ ,  $d_s$ , and  $d_{sc}$ , respectively.  $l_t$  and  $l_c$  denote semi-distances between bogies and wheelsets.  $F_{L1sxi}$  and  $F_{R1sxi}$  are the longitudinal forces of the left and right first suspension at the  $j$ -th wheelset, with analogous expressions for the  $y$  and  $z$  axes. Similarly,  $F_{L2sxi}$  and  $F_{R2sxi}$  denote longitudinal forces for the second suspension, and  $F_{Lsxi}$  and  $F_{Rsxi}$  for the anti-hunting dampers at the  $i$ -th bogie. Rotations about the  $x$ ,  $y$ , and  $z$  axes are given by  $\phi$ ,  $\beta$ , and  $\Psi$ , respectively, with  $v$  representing train speed and  $\Omega$  the nominal rolling angular velocity of the wheelset.

According to the principles of beam and rod dynamics, the longitudinal, torsional, lateral, and vertical vibrations of rail are considered simultaneously. The axial and torsional vibrations of the rail are regarded as fixed-end constraint rods, and the bending vibrations of the rails are assumed as simply supported Euler-Bernoulli beams.

$$\left\{ \begin{array}{l} m_r \frac{\partial^2 X_r(x, t)}{\partial t^2} - E_r A_r \frac{\partial^2 X_r(x, t)}{\partial x^2} = - \sum_{i=1}^{N_f} F_{rsxi}(t) \delta(x - x_{fi}) - \sum_{j=1}^{N_w} F_{wrxj}(t) \delta(x - x_{wj}) \\ \rho_r I_{r0} \frac{\partial^2 \phi_r(x, t)}{\partial t^2} - G_r I_{rt} \frac{\partial^2 \phi_r(x, t)}{\partial x^2} = - \sum_{i=1}^{N_f} M_{rsxi}^e(t) \delta(x - x_{fi}) - \sum_{j=1}^{N_w} M_{wrxj}^e(t) \delta(x - x_{wj}) \\ E_r I_{rz} \frac{\partial^4 Y_r(x, t)}{\partial x^4} + m_r \frac{\partial^2 Y_r(x, t)}{\partial t^2} = - \sum_{i=1}^{N_f} F_{rsyi}(t) \delta(x - x_{fi}) - \sum_{j=1}^{N_w} F_{wryj}(t) \delta(x - x_{wj}) \\ E_r I_{ry} \frac{\partial^4 Z_r(x, t)}{\partial x^4} + m_r \frac{\partial^2 Z_r(x, t)}{\partial t^2} = - \sum_{i=1}^{N_f} F_{rszi}(t) \delta(x - x_{fi}) + \sum_{j=1}^{N_w} F_{wrzj}(t) \delta(x - x_{wj}) \end{array} \right. \quad (A9)$$

where  $E_r A_r$ ,  $E_r I_{rz}$ ,  $E_r I_{ry}$ , and  $G_r I_{rt}$  are the axial stiffness, vertical bending stiffness, lateral bending stiffness and torsional stiffness of the rail, respectively;  $I_{r0}$  is the polar moment of inertia of the rail;  $m_r$  is the mass of the rail per unit length;  $\rho_r$  is the mass density;  $x_{fi}$  and  $x_{wj}$  are the positions of the  $i$ -th fastener and  $j$ -th wheelset, respectively;  $N_f$  and  $N_w$  are the total numbers of fasteners and wheelsets, respectively;  $F_{rsxi}$ ,  $F_{rsyi}$ , and  $F_{rszi}$  are the longitudinal, lateral and vertical forces between rail and track slab, respectively;  $M_{rsxi}^e$  and  $M_{wrxj}^e$  are the equivalent moments on the rails of the forces caused by the fasteners and the wheel-rail, respectively.

## Appendix B. Vehicle-track system dynamic parameters

**Table I**  
Main parameters of the subway Vehicle.

Parameter	Vehicle	Unit
Mass of car body/bogie frame/wheelset	34,400/2722/1350	kg
Mass moment of inertia of car body about x / y / z axis	112/862/783	t·m <sup>2</sup>
Mass moment of inertia of bogie frame about x / y / z axis	1260/1600/2810	kg·m <sup>2</sup>
Mass moment of inertia of wheelset about x / y / z axis	856/114/872	kg·m <sup>2</sup>
Vertical/Lateral/Longitudinal stiffness of primary suspension	1.32/5.6/7.66	MN/m
Vertical/Lateral/Longitudinal damping of primary suspension	52.6/0/0	kN·s/m

(continued on next page)

**Table I (continued)**

Parameter	Vehicle	Unit
Vertical/Lateral/Longitudinal stiffness of secondary suspension	0.38/0.18/0.18	MN/m
Vertical/Lateral/Longitudinal damping of secondary suspension	13.9/4.6/4.6	kN·s/m
Semi-longitudinal distance between wheelsets in a bogie	7.85	m
Semi-longitudinal distance between bogie frames	1.25	m
Semi-transverse distance between primary/secondary suspension	0.965/0.925	m
Nominal rolling radius of wheel	0.42	m

**Table II**  
Main parameters of the track.

Component	Parameter	Value	Unit
Fastener (MST, FST)	Fastener spacing	0.6	m
	Vertical/Lateral/Longitudinal stiffness	30/25/25	MN/m
	Vertical/Lateral/Longitudinal damping	25/25/25	kN·s/m
	Length/Width/Thickness	25.2/3.3/0.4	m
Slab (FST)	Density	2500	kg/m <sup>3</sup>
	Elastic modulus	36,000	MPa
	Poisson's ratio	0.25	—
Steel spring (FST)	Horizontal/ Longitudinal spacing	1.89/1.2	m
	Vertical/Lateral/Longitudinal stiffness	6.6/4.9/4.9	MN/m
	Vertical/Lateral/Longitudinal damping	10/10/10	kN·s/m

## References

- [1] Zhai W. Vehicle–track coupled dynamics theory and applications. Springer Singapore; 2020. <https://doi.org/10.1080/00423114.2020.1827153>.
- [2] Qu S, Zhao L, Yang J, Wu Z, Zhu S, Zhai W. Numerical analysis of engineered metabARRIER effect on ground vibration induced by underground high-speed train. Soil Dyn Earthq Eng 2023;164:107580. <https://doi.org/10.1016/j.soildyn.2022.107580>.
- [3] Bhalla S, Yang YW, Zhao J, Soh CK. Structural health monitoring of underground facilities - technological issues and challenges. Tunn Undergr Sp Technol 2005;20: 487–500. <https://doi.org/10.1016/j.tust.2005.03.003>.
- [4] Li M, Jing X. Novel tunable broadband piezoelectric harvesters for ultralow-frequency bridge vibration energy harvesting. Appl Energy 2019;255. <https://doi.org/10.1016/j.apenergy.2019.113829>.
- [5] Wischke M, Masur M, Kröner M, Woias P. Vibration harvesting in traffic tunnels to power wireless sensor nodes. Smart Mater Struct 2011;20. <https://doi.org/10.1088/0964-1726/20/8/085014>.
- [6] Yang Y, Tang L, Li H. Vibration energy harvesting using macro-fiber composites. Smart Mater Struct 2009;18. <https://doi.org/10.1088/0964-1726/18/11/115025>.
- [7] Wei C, Jing X. A comprehensive review on vibration energy harvesting: modelling and realization. Renew Sustain Energy Rev 2017;74:1–18. <https://doi.org/10.1016/j.rser.2017.01.073>.
- [8] Pan H, Qi L, Zhang Z, Yan J. Kinetic energy harvesting technologies for applications in land transportation: a comprehensive review. Appl Energy 2021; 286. <https://doi.org/10.1016/j.apenergy.2021.116518>.
- [9] Bosso N, Magelli M, Zampieri N. Application of low-power energy harvesting solutions in the railway field: a review. Veh Syst Dyn 2021;59:841–71. <https://doi.org/10.1080/00423114.2020.1726973>.
- [10] Hosseinkhani A, Younesian D, Eghbali P, Moayedizadeh A, Fassih A. Sound and vibration energy harvesting for railway applications: a review on linear and nonlinear techniques. Energy Rep 2021;7:852–74. <https://doi.org/10.1016/j.egyr.2021.01.087>.
- [11] Yuan W, Frey HC. Potential for metro rail energy savings and emissions reduction via eco-driving. Appl Energy 2020;268:1–13. <https://doi.org/10.1016/j.apenergy.2020.114944>.
- [12] Zhao X, Wei G, Li X, Qin Y, Xu D, Tang W, et al. Self-powered triboelectric nano vibration accelerometer based wireless sensor system for railway state health monitoring. Nano Energy 2017;34:549–55. <https://doi.org/10.1016/j.nanoen.2017.02.036>.
- [13] Zhang X, Zhang Z, Pan H, Salman W, Yuan Y, Liu Y. A portable high-efficiency electromagnetic energy harvesting system using supercapacitors for renewable energy applications in railroads. Energ Conver Manage 2016;118:287–94. <https://doi.org/10.1016/j.enconman.2016.04.012>.
- [14] Safaei M, Sodano HA, Anton SR. A review of energy harvesting using piezoelectric materials: state-of-the-art a decade later (2008–2018). Smart Mater Struct 2019;28. <https://doi.org/10.1088/1361-665X/ab36e4>.
- [15] Saadon S, Sidek O. A review of vibration-based MEMS piezoelectric energy harvesters. Energ Conver Manage 2011;52:500–4. <https://doi.org/10.1016/j.enconman.2010.07.024>.
- [16] Hu G, Tang L, Liang J, Lan C, Das R. Acoustic-elastic metamaterials and phononic crystals for energy harvesting: a review. Smart Mater Struct 2021;30. <https://doi.org/10.1088/1361-665X/ac0cbc>.
- [17] Dong L, Zuo J, Wang T, Xue W, Wang P, Li J, et al. Enhanced piezoelectric harvester for track vibration based on tunable broadband resonant methodology. Energy 2022;254:124274. <https://doi.org/10.1016/j.energy.2022.124274>.
- [18] Yang F, Gao M, Wang P, Zuo J, Dai J, Cong J. Efficient piezoelectric harvester for random broadband vibration of rail. Energy 2021;218:119559. <https://doi.org/10.1016/j.energy.2020.119559>.
- [19] Gao MY, Wang P, Cao Y, Chen R, Liu C. A rail-borne piezoelectric transducer for energy harvesting of railway vibration. J Vibroeng 2016;18:4647–63. <https://doi.org/10.21595/jve.2016.16938>.
- [20] Wang J, Cao Y, Xiang H, Zhang Z, Liang J, Li X, et al. A piezoelectric smart backing ring for high-performance power generation subject to train induced steel-spring fulcrum forces. Energ Conver Manage 2022;257:115442. <https://doi.org/10.1016/j.enconman.2022.115442>.
- [21] Hou W, Zheng Y, Guo W, Pengcheng G. Piezoelectric vibration energy harvesting for rail transit bridge with steel-spring floating slab track system. J Clean Prod 2021;291. <https://doi.org/10.1016/j.jclepro.2020.125283>.
- [22] Kansal A, Hsu J, Zahedi S, Srivastava MB. Power Management in Energy Harvesting Sensor Networks. ACM Trans Embed Comput Syst 2007;6:32. <https://doi.org/10.1145/1274858.1274870>.
- [23] Yang Y, Tang L. Equivalent circuit modeling of piezoelectric energy harvesters. J Intell Mater Syst Struct 2009;20:2223–35. <https://doi.org/10.1177/1045389X09351757>.
- [24] Sun R, Zhou S, Cheng L. Ultra-low frequency vibration energy harvesting: mechanisms, enhancement techniques, and scaling laws. Energ Conver Manage 2023;276. <https://doi.org/10.1016/j.enconman.2022.116585>.
- [25] Wang Y, Li S, Wang P, Gao M, Ouyang H, He Q, et al. A multifunctional electromagnetic device for vibration energy harvesting and rail corrugation sensing. Smart Mater Struct 2021;30. <https://doi.org/10.1088/1361-665X/ac31c5>.
- [26] Erturk A, Inman DJ. Issues in mathematical modeling of piezoelectric energy harvesters. Smart Mater Struct 2008;17. <https://doi.org/10.1088/0964-1726/17/6/065016>.
- [27] Zachariae R, Tooole MSO. Modeling, validation, and performance of low-frequency piezoelectric energy harvesters. J Intell Mater Syst Struct 2015;6:10–10.
- [28] Erturk A, Inman DJ. On mechanical modeling of cantilevered piezoelectric vibration energy harvesters. J Intell Mater Syst Struct 2008;19:1311–25. <https://doi.org/10.1177/1045389X07085639>.
- [29] DuToit NE, Wardle BL, Kim SG. Design considerations for MEMS-scale piezoelectric mechanical vibration energy harvesters. Integr Ferroelectr 2005;71:121–60. <https://doi.org/10.1080/1058458059064574>.
- [30] Peralta P, Ruiz RO, Natarajan S, Atroschenko E. Parametric study and shape optimization of piezoelectric energy harvesters by isogeometric analysis and kriging metamodeling. J Sound Vib 2020;484. <https://doi.org/10.1016/j.jsv.2020.115521>.
- [31] De Marqui Junior C, Erturk A, Inman DJ. An electromechanical finite element model for piezoelectric energy harvester plates. J Sound Vib 2009;327:9–25. <https://doi.org/10.1016/j.jsv.2009.05.015>.

- [32] Dietl JM, Wickenheiser AM, Garcia E. A Timoshenko beam model for cantilevered piezoelectric energy harvesters. *Smart Mater Struct* 2010;19. <https://doi.org/10.1088/0964-1726/19/5/055018>.
- [33] Erturk A, Inman DJ. An experimentally validated bimorph cantilever model for piezoelectric energy harvesting from base excitations. *Smart Mater Struct* 2009;18. <https://doi.org/10.1088/0964-1726/18/2/025009>.
- [34] Rafique S, Bonello P. Experimental validation of a distributed parameter piezoelectric bimorph cantilever energy harvester. *Smart Mater Struct* 2010;19. <https://doi.org/10.1088/0964-1726/19/9/094008>.
- [35] Wang J, Yurchenko D, Hu G, Zhao L, Tang L, Yang Y. Perspectives in flow-induced vibration energy harvesting. *Appl Phys Lett* 2021;119. <https://doi.org/10.1063/5.0063488>.
- [36] Chen S, Zhao L. A quasi-zero stiffness two degree-of-freedom nonlinear galloping oscillator for ultra-low wind speed aeroelastic energy harvesting. *Appl Energy* 2023;331. <https://doi.org/10.1016/j.apenergy.2022.120423>.
- [37] Wang J, Geng L, Ding L, Zhu H, Yurchenko D. The state-of-the-art review on energy harvesting from flow-induced vibrations. *Appl Energy* 2020;267. <https://doi.org/10.1016/j.apenergy.2020.114902>.
- [38] Zhao L, Yang Y. An impact-based broadband aeroelastic energy harvester for concurrent wind and base vibration energy harvesting. *Appl Energy* 2018;212:233–43. <https://doi.org/10.1016/j.apenergy.2017.12.042>.
- [39] Zhao C, Hu G, Li X, Liu Z, Yuan W, Yang Y. Wide-bandwidth triboelectric energy harvester combining impact nonlinearity and multi-resonance method. *Appl Energy* 2023;348. <https://doi.org/10.1016/j.apenergy.2023.121530>.
- [40] Zhang Q, Liu Z, Jiang X, Peng Y, Zhu C, Li Z. Experimental investigation on performance improvement of cantilever piezoelectric energy harvesters via escapement mechanism from extremely low-frequency excitations. *Sustain Energy Technol Assess* 2022;53. <https://doi.org/10.1016/j.seta.2022.102591>.
- [41] Tri Nguyen H, Genov DA, Bardawell H. Vibration energy harvesting using magnetic spring based nonlinear oscillators: design strategies and insights. *Appl Energy* 2020;269. <https://doi.org/10.1016/j.apenergy.2020.115102>.
- [42] Zhao Z, Zhang B, Li Y, Bao C, Wang T. A novel piezoelectric energy harvester of noncontact magnetic force for a vehicle suspension system. *Energy Sci Eng* 2022;1133–47. <https://doi.org/10.1002/ese3.1377>.
- [43] Tang L, Yang Y, Soh CK. Improving functionality of vibration energy harvesters using magnets. *J Intell Mater Syst Struct* 2012;23:1433–49. <https://doi.org/10.1177/1045389X12443016>.
- [44] Tang L, Yang Y. A nonlinear piezoelectric energy harvester with magnetic oscillator. *Appl Phys Lett* 2012;101. <https://doi.org/10.1063/1.4748794>.
- [45] Kuang Y, Chew ZJ, Ruan T, Lane T, Allen B, Nayar B, et al. Magnetic field energy harvesting from the traction return current in rail tracks. *Appl Energy* 2021;292. <https://doi.org/10.1016/j.apenergy.2021.116911>.
- [46] Liu M, Zhang Y, Fu H, Qin Y, Ding A, Yeatman EM. A seesaw-inspired bistable energy harvester with adjustable potential wells for self-powered internet of train monitoring. *Appl Energy* 2023;337. <https://doi.org/10.1016/j.apenergy.2023.120908>.
- [47] Gao M, Wang P, Cao Y, Chen R, Cai D. Design and verification of a rail-borne energy harvester for powering wireless sensor networks in the railway industry. *IEEE Trans Intell Transp Syst* 2017;18:1596–609. <https://doi.org/10.1109/TITS.2016.2611647>.
- [48] Gao M, Wang P, Wang Y, Yao L. Self-powered ZigBee wireless sensor nodes for railway condition monitoring. *IEEE Trans Intell Transp Syst* 2018;19:900–9. <https://doi.org/10.1109/TITS.2017.2709346>.
- [49] Lu Z, Hu Z, Yao H, lin, Liu J. Field evaluation and analysis of road subgrade dynamic responses under heavy duty vehicle. *Int J Pavement Eng* 2018;19:1077–86. <https://doi.org/10.1080/10298436.2016.1240560>.
- [50] Wang ZL, Chen J, Lin L. Progress in triboelectric nanogenerators as a new energy technology and self-powered sensors. *Energ Environ Sci* 2015;8:2250–82. <https://doi.org/10.1039/c5ee01532d>.
- [51] Khan FU, Qadir MU. State-of-the-art in vibration-based electrostatic energy harvesting. *J Micromech Microeng* 2016;26. <https://doi.org/10.1088/0960-1317/26/10/103001>.
- [52] Ahmad MM, Khan FU. Review of vibration-based electromagnetic-piezoelectric hybrid energy harvesters. *Int J Energy Res* 2021;45:5058–97. <https://doi.org/10.1002/er.6253>.
- [53] Hu Y, Wang X, Qin Y, Li Z, Wang C, Wu H. A robust hybrid generator for harvesting vehicle suspension vibration energy from random road excitation. *Appl Energy* 2022;309. <https://doi.org/10.1016/j.apenergy.2021.118506>.
- [54] Han Y, He L, Zheng X, Hu R, Huang H, Zhao H. Composite piezoelectric-electromagnetic synchronously powering and sensing device for vehicle monitoring. *Energ Conver Manage* 2023;286:1–14. <https://doi.org/10.1016/j.enconman.2023.117040>.
- [55] Gao M, Cong J, Xiao J, He Q, Li S, Wang Y, et al. Dynamic modeling and experimental investigation of self-powered sensor nodes for freight rail transport. *Appl Energy* 2020;257. <https://doi.org/10.1016/j.apenergy.2019.113969>.
- [56] Ali SF, Friswell MI, Adhikari S. Piezoelectric energy harvesting with parametric uncertainty. *Smart Mater Struct* 2010;19. <https://doi.org/10.1088/0964-1726/19/10/105010>.
- [57] Peralta-Braz P, Alamdari MM, Ruiz RO, Atroschenko E, Hassan M. Design optimisation of piezoelectric energy harvesters for bridge infrastructure. *Mech Syst Signal Proc* 2023;205. <https://doi.org/10.1016/j.ymssp.2023.110823>.
- [58] Hu G, Tang L, Liang J, Das R. Modelling of a cantilevered energy harvester with partial piezoelectric coverage and shunted to practical interface circuits. *J Intel Mater Syst Struct* 2019;30:1896–912. <https://doi.org/10.1177/1045389X19849269>.
- [59] Gilbert JM, Balouchi F. Comparison of energy harvesting systems for wireless sensor networks. *Int J Autom Comput* 2008;5:334–47. <https://doi.org/10.1007/s11633-008-0334-2>.
- [60] Lyshевski SE. High-power density miniscale power generation and energy harvesting systems. *Energ Conver Manage* 2011;52:46–52. <https://doi.org/10.1016/j.enconman.2010.06.030>.
- [61] Slowik A. Particle swarm optimization. In: Proc. ICNN'95 - Int. Conf. Neural networks. Perth, WA, Australia: IEEE; 1995. p. 1942–8. [https://doi.org/10.1007/978-3-319-46173-1\\_2](https://doi.org/10.1007/978-3-319-46173-1_2).
- [62] Krishna K, Murty MN. Genetic K-means algorithm. *IEEE Trans Syst Man Cybern* 1999;29:433–9.
- [63] Shahapure KR, Nicholas C. Cluster quality analysis using silhouette score. In: Proc - 2020 IEEE 7th Int Conf Data Sci Adv Anal DSAA 2020; 2020. p. 747–8. <https://doi.org/10.1109/DSAA49011.2020.00096>.
- [64] Dai HL, Abdelkefi A, Wang L. Piezoelectric energy harvesting from concurrent vortex-induced vibrations and base excitations. *Nonlinear Dyn* 2014;77:967–81. <https://doi.org/10.1007/s11071-014-1355-8>.
- [65] Zhai W, Wang K, Cai C. Fundamentals of vehicle-track coupled dynamics. *Veh Syst Dyn* 2009;47:1349–76. <https://doi.org/10.1080/00423110802621561>.
- [66] Luo J, Zhu S, Zhai W. An advanced train-slab track spatially coupled dynamics model: theoretical methodologies and numerical applications. *J Sound Vib* 2021;501:116059. <https://doi.org/10.1016/j.jsv.2021.116059>.
- [67] Zhai WM. Two simple fast integration methods for large-scale dynamic problems in engineering. *Int J Numer Methods Eng* 1996;39:4199–214. [https://doi.org/10.1002/\(SICI\)1097-0207\(19961230\)39:24<4199::AID-NME39>3.0.CO;2-Y](https://doi.org/10.1002/(SICI)1097-0207(19961230)39:24<4199::AID-NME39>3.0.CO;2-Y).
- [68] Qu S, Yang J, Zhu S, Zhai W, Kouroussis G, Zhang Q. Experimental study on ground vibration induced by double-line subway trains and road traffic. *Transp Geotech* 2021;29. <https://doi.org/10.1016/j.trgeo.2021.100564>.
- [69] Qu S, Yang J, Zhu S, Zhai W, Kouroussis G, Yang J, et al. A hybrid methodology for predicting train-induced vibration on sensitive equipment in far-field buildings. *Transp Geotech* 2021;31. <https://doi.org/10.1016/j.trgeo.2021.100682>.
- [70] Dong L, Hu G, Yu J, Zhao C, Qu S, et al. Maximizing onboard power generation of large-scale railway vibration energy harvesters with intricate vehicle-harvester-circuit coupling relationships. *Appl Energy* 2023;254:115228. <https://doi.org/10.1016/j.apenergy.2023.121388>.
- [71] Zuo J, Dong L, Yang F, et al. Energy harvesting solutions in railway industry: a comprehensive review. *Renew Energ* 2023;202:56–87. <https://doi.org/10.1016/j.renene.2022.11.008>.
- [72] Wowk V. Vibration energy n.d. Retrieved from [https://www.machinedyn.com/docs/articles/Vibration\\_Energy.pdf](https://www.machinedyn.com/docs/articles/Vibration_Energy.pdf).